Original Article

Design of highly anti-corrosive electroless plated Ni−P/modified halloysite nanotubes nanocomposite coating

Eman M. Fayyad[**,1], Khouloud Jlassi, Mostafa H. Sliem, Fatma Nabhan, Aboubakr M. Abdullah[*]

Center for Advanced Materials, Qatar University, Doha 2713, Qatar

ABSTRACT

Halloysite nanotubes (HNTs) and their modifications with either NH_2 (HNT-NH_2) or NH_2/Polypyrrole (HNT−NH_2−PPy) were electroless-deposited into the NiP matrix for the first time to form NiP/HNT, NiP/HNT-NH_2 and NiP/HNT−NH_2−PPy nanocomposite coatings. The as-prepared nanocomposite coatings were heat-treated at 400 °C for 1 h. The transformation in microstructure, nanoindentation, Vicker's micro-hardness, surface morphology, and anti-corrosive properties of all prepared composite coatings were compared to the HNT-free (NiP) coating. Incorporating HNTs in the NiP coating made an appreciable enhancement in the hardness and corrosion resistance. Using the electrochemical impedance spectroscopy technique (EIS), the NiP/HNT-NH_2 and NiP/HNT−NH_2−PPy coatings showed more significant levels of enhancement in anticorrosion performance, offering about 16.5% and 25.4%, respectively, an increase in the inhibition efficiency of unmodified one (NiP/HNT), reached to 73 and 82%. Moreover, the modified HNT coatings revealed slightly high levels of betterment in microhardness, about 9% and 5.4% for HNT modification with NH_2 and NH_2-PPy, respectively. In addition, the heat treatment extra improved the hardness and the corrosion resistance of all HNTs nanocomposite coatings compared to HNT-free coating. Furthermore, the heat-treated NiP/HNT has the highest protection efficiency reached to about 95%, based on the polarization measurements. This momentous improvement in the hardness and electrochemical properties reflects the effect of adding the pristine and the modified HNTs into the NiP matrix, resulting in the development of high-performance NiP/HNT-NH_2 and NiP/HNT−NH_2−PPy composite coatings facilitating their use in various industries.

* Corresponding author.
** Corresponding author.
   E-mail addresses: emfayad@qu.edu.qa (E.M. Fayyad), abubakr_2@yahoo.com (A.M. Abdullah).
 [1] Permanent address: Physical Chemistry Department, National Research Centre, P.O. Box 12622, Dokki, Cairo, Egypt.

1. Introduction

A promising approach to protect environmentally soft materials from prolonged use is electroless nickel (EN)-based plating. In many ways, electroless plating is similar to a chemical reduction process despite their significant differences. Electroless plating encompasses the catalytic reduction of metallic ions in a reducing agent-containing aqueous solution [1—4]. Therefore, the metal's subsequent deposition occurs in the absence of any external energy source. Some of its distinguished advantages are its highly eco-friendly electrochemical and mechanical characteristics. Electroless nickel-phosphorus (E-NiP) coating is about 95% of EN-based coatings [5]. They are widely used in industry and engineering applications due to their desirable characteristics, including excellent hardness, uniform coating, promising wear, corrosion resistance, high adhesion, and weldability [6,7]. The addition of certain solid particles into the E-NiP coating is attributable to the quest to enhance their characteristics further. In the latest years, with tremendous evolution in nanotechnology, thanks to some reinforcements that are utilized for the improvement of the E-NiP characteristics, like Al_2O_3 [8], W [9], C_3N_4 [10,11], TiN [12], TiO_2 [13], SiO_2 [14], B.N. [15], TiNi [16], SiC [17], etc. Therefore, the resulting E-NiP composite coatings mishmash the unique features of both the conventional electroless nickel deposits and those of the added solid particles, which helps the creation of unique composite coatings and offers special applications. Undeniably, one must pay attention to the surface conditions and microstructures of the composite coatings, which are the main factors affecting their electrochemical and mechanical properties [18,19]. These factors are highly dependent on other parameters like the type, size, and concentration of the reinforcement particles and on some treatment processes, for instance, heat treatment of the coatings. The heat treatment significantly changes the NiP coating from amorphous to nanocrystalline [20] and in the reinforced NiP coating surface conditions [21,22].

Halloysite nanotubes (HNTs) are naturally occurring hollow nanotube clay. It is primarily made of a two-layered aluminosilicate in a stoichiometric ratio of 1:1. One layer consists of an alumina octahedron sheet, and the other is a silica tetrahedron sheet with the composition of $[Al_2Si_2O_5(OH)_4 \cdot 2H_2O]$. The chemical characteristics of the superficial layers of the HNTs' are comparable to the characteristics of SiO_2, but the characteristics of the central innermost cylinder might be linked with the characteristics of Al_2O_3 [23]. Due to the chemical and physical characteristics of HNTs, they have been used in various applications in fields like optics [24], catalysis [25], biological systems [26], drug delivery [27], electronics [28], and energy storage [29]. Moreover, another application of HNTs is their utilization as a new type of filler for polymers, such as polyvinyl alcohol, polypropylene, and epoxy, to enhance the thermal and mechanical characteristics of the composites [30,31]. In addition, HNTs are used to create an innovative form of active protective coatings, which is called self-healing coating, in which the HNTs are used as nanocontainers and filled with suitable corrosion inhibitors that are liberated, under certain conditions, in a controllable

way [32—34] An extra advantage of halloysite particles is the easily accessible, modification and inexpensive in comparison with other materials such as CNTs. Also, HNTs are easily incorporated into the polymer/metal matrix or the solutions due to their geometry, which looks like rods that never interlace. As a result, the halloysite-based composites are quickly fabricated through the electroless deposition. Despite that, only a single study examined the influence of the direct use of HNTs on the mechanical, electrochemical, and tribological characteristics of electroless Ni—P coating so far [35]. Notably, the use of modified HNTs has not been previously studied in the electroless coating.

Thus, this paper comparatively analyzed the composite coating's structure morphology, composition, and phase modification in the presence of HNTs and modified HNTs using the APTES (3-aminopropyltriethoxysilane) (HNT-NH_2) and polypyrrole (HNT—NH_2—PPy) into the NiP matrix. APTES contains NH_2 that will serve as anchoring sites for the pyrrole under UV irradiation and in the presence of the photosensitizer. In addition, the microhardness and corrosion resistance behavior of HNTs and modified HNTs reinforced composite coatings have been studied. Furthermore, the influence of heat treatment on the structure morphology, composition, roughness, microhardness, and electrochemical characteristics of the different reinforced composite coatings has been examined.

2. Experimental

2.1. Materials and specimen treatment

$20 \times 15 \times 5$ mm of pipeline steel (API X120) specimens purchased from Tianjin Tiangang Guanye Co. Ltd., (Tianjin, China) have been utilized for the substrate. The specimen constituent is 0.13% C, 0.54% Mn, 0.02% Ni, 0.1% Si, 0.04% Cr, 0.02% Cu, 0.01% Mo, 0.25% V and the balance is Fe. Differing grit polishing papers were used to grind the specimens. Three μm micro-polish suspension of alumina was used to ultra-polish the specimens. Fifteen minutes (min) of acetone bath was used for degreasing the specimens ultrasonically. Finally, the specimens were submerged for 5 min at 80 ± 5 °C in a solution containing 30 g L^{-1} Na_3PO_4, 30 g L^{-1} Na_2CO_3, and 50 g L^{-1} NaOH. After that, they were etched for 20 s in a solution of 15 wt % H_2SO_4. All solvents are from analytical grade and purchased from Sigma—Aldrich. After every mechanical and chemical pretreatment step, distilled water was used to swill the specimens carefully.

2.2. HNTs preparation, modification, and characterization

Pyrrole, Silver nitrate, APTES (3-aminopropyltriethoxysilane), and commercial/purified HNT clay were purchased from Sigma-Aldrich. Our team prepared the hybrid nanocomposites [36]; HNT-NH_2 using the APTES as a coupling agent, and the HNT—NH_2—PPy were prepared by polymerization of pyrrole, and using silver nitrate as a photosensitizer, subsequently, used as a platform for the pyrrole in situ polymerization. Fig. 1 summarizes the rational design of the HNT—NH_2—PPy. The HNT was first silanized using the APTES.
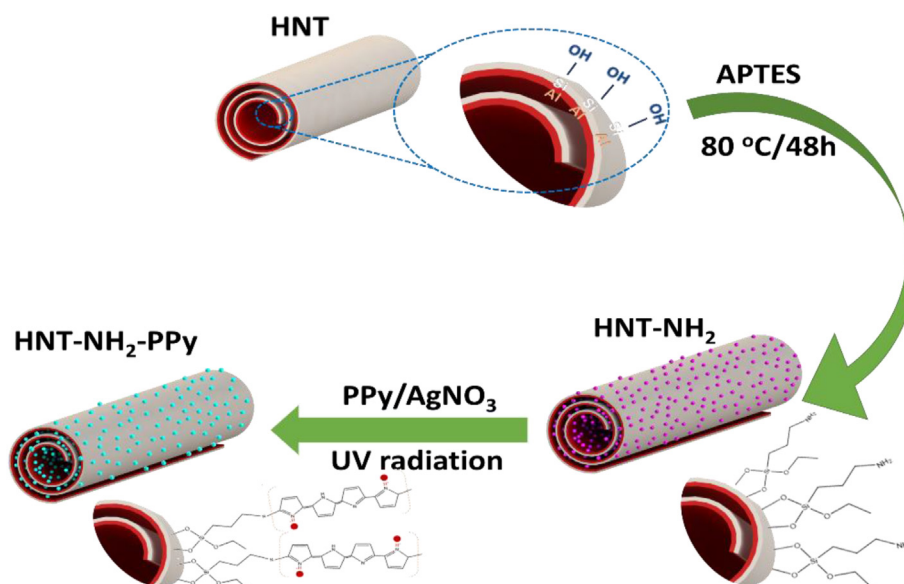
Fig. 1 — **Graphical summary for modification of HNTs with NH$_2$ (HNT-NH$_2$) and further modification with NH$_2$-PPy (HNT−NH$_2$−PPy). APTES is an abbreviation for 3-aminopropyltriethoxy-silane. PPy is an abbreviation for polypyrrole.**

Prior to all modifications, 4 g of commercial and purified HNT were dispersed in water (400 ml) for 5 min. To the clay suspension, a solution of 3-aminopropyltriethoxysilane (228 mg) in 50 ml of ethanol/acetic acid (95/5 v/v) mixture was added. Silanization of HNT was left to proceed for 48 h at 80 °C. The silanized Halloysite (HNT-NH$_2$) was washed four times with deionized water and ethanol to remove the excess of reactants and then redispersed in ethanol. The HNT-NH$_2$ was finally dried at 80 °C for 48 h, then (2 g) of the obtained HNT-NH$_2$, was dispersed for 10 min in Aqueous AgNO$_3$ solution (1.68 g in 200 ml) under vigorous stirring. At last, pyrrole aqueous solution (0.5 mol/L) was injected and stirred, and the glass vessel with HNT suspension was placed 13 cm below the six lamps of the UV-reactor (Spectrolinker 1500) and illuminated at 365 nm for 1 h; the power density was ~5 mW/cm^2. Photopolymerisation was conducted under stirring. After UV exposure, the samples were thoroughly cleaned with deionized water and ethanol to remove the unreacted species. Finally, the samples were dried for 8 h at 40 °C in an oven.

A "Nova NanoSEM 450" scanning electron microscope (SEM) from Thermo Fisher Scientific, Eindhoven, The Netherlands, and transmission electron microscopy (TEM) (FEI, TALOS F200X, USA) were used to distinguish the morphology of the prepared Halloysite and the modified ones. Energy−dispersive X-ray spectroscopy (EDX) (Bruker, Leiderdorp, The Netherlands) that is connected with SEM and the X-ray Photoelectron Spectroscopy (XPS) analysis (ESCALAB 250X equipment from ThermoFisher Scientific, Waltham, MA, USA) were performed to determine the surface composition of the as-prepared and the modified HNTs. The XPS was done with 1 eV energy resolution and AlKα excitation radiation (25 W, hυ = 1486.5 eV). Thermal decomposition was tested using PerkinElmer TGA-4000. About 15−30 mg of the sample

was heated from 30 °C to 800 °C at a heating rate of 10 °C/min under a nitrogen atmosphere.

2.3. Coating preparation

The electroless Nichem 3100 plating solution of NiP was used to submerge the pretreated specimens directly. It is from Atotech Deutschland GmbH (Berlin, Germany) and is made of nickel sulfate and sodium hypophosphite. The former is the main salt, and the latter is the reducing agent. 1 g of each readied HNT, HNT-NH$_2$, and HNT−NH$_2$−PPy was individually put into 1 L of the deposition solution. Firstly, an ultrasonicator from Fisher Scientific U.K. Ltd. (Loughborough, U.K.) was used to mix the composite electroless solution, e.g. (NiP/HNT), for 3 h at room temperature. After that, a thermal stirring magnetic mantel bought from Cole−Parmer (Staffordshire, U.K.) was used to stir the electroless solution for 2 h at 300 rpm. The deposition solution was set to a temperature of 87 °C. The pH of the electroless solution was 4.5, preserved during the deposition time by adding small amounts of NH$_4$OH to the deposition bath. The coated specimens were washed using deionized water after the plating time. In the end, using blowing air, the coated specimens were dried. A vacuum furnace (MTI Corporation, Richmond, CA, USA), at 20 °C/min heating and cooling rate, was used for annealing (HT) some specimens at 400 °C for 1 h.

2.4. Coatings characterization

2.4.1. Morphology, composition, and structural feature

A Miniflex2 Desktop X-ray diffractometry (XRD), from Tokyo, Japan, was used to examine the various phases and structures of the reinforced coatings. SEM was used to identify the change in the reinforced coatings morphologies. EDX was

utilized to recognize the coatings' elemental compositions. The coated samples were scanned at 2Ө angles from 30° to 60°.

2.4.2. Microhardness

In order to find the microhardness of the coated samples, both Nano-indentation and Vickers microhardness testers were utilized. F.M.−ARS9000, Future−Tech Corp Vickers hardness machine from Tokyo, Japan, was used. A load of 200 g was utilized through a holding time of 10 s. The outcomes were repeated fivefold, and an average was acquired. The experiments of nano-indentation have been done at room temperature (R.T.) utilizing an MFP−3D Nano Indenter system attached to a typical Berkovich indenter tip of the diamond. The exerted forces and the penetration depths utilized were in the mN range and the nm to μm, respectively. Thus, it was possible to find the hardness (H) straightforwardly. The indentation was created using a maximum load of about 1 mN, through 200 μNs^{-1} loadings and unloading rate and 5 s settling time at the maximum load. All the tests were repeated for 6 indentations, and an average was acquired.

2.4.3. Roughness and hydrophobicity

An AFM (A MFP−3D Asylum Research, Santa Barbara, CA, USA) was used to quantify the surface roughness of the coated specimens. The AFM was attached to a silicon probe (Al reflex coated Veeco model−OLTESPA, Olympus, Tokyo, Japan) set at a resonant frequency of 70 kHz and a spring constant of 2 Nm^{-1}. All the measurements were found at standard conditions utilizing Standard Topography A.C. in the air. A contact angle measurement was utilized to investigate the hydrophobicity of the different coatings (OCA 35, Data Physics, Germany). In this experiment, we dropped a tiny droplet of deionized water (2 μL) on the coated specimen's surface. Then, the droplet's shape was pictured using the digital camera (Canon-type). Finally, the tangent to the droplet was drawn, and the angle between it and the coating's surface was measured. For reducibility, measuring the contact angle for each coating was repeated at least three times.

2.4.4. Electrochemical properties

For the study of the electrochemical performance of the various reinforced coatings, at room temperature, in a brine solution of NaCl (3.5 wt %), both potentiodynamic polarization (P·P.) and electrochemical impedance spectroscopy (EIS) were utilized. The electrochemical experiments were done using 3000 Gamry workstations (Gamry Instruments, Warminster, PA, USA). A conventional flat corrosion cell was utilized, including the working, reference, and counter electrodes. An Ag/AgCl electrode and a platinum wire were utilized as the reference and the counter electrodes, respectively. The coated surface area exposed to the electrolyte (NaCl) was 1 cm^2. The utilized frequency range for the EIS experiments was 1×10^{-2}−1×10^5 Hz alongside an A.C. amplitude of 10 mV. After attaining the open circuit potential (OCP), all recorded data was found. In the P.P. experiments, a 0.167 mV s^{-1} sweep rate and ±250 mV sweep potential range were employed versus the OCP. The corrosion current (i_{corr}) and the corrosion potential (E_{corr}) can be calculated from the Tafel curve by extrapolating the straight-line section of the anodic and cathodic branches.

3. Results and discussion

3.1. HNTs characterization

3.1.1. Morphology, composition, and structural features (SEM, TEM, EDX, and XPS)

Fig. 2(a−f) shows the TEM and SEM images of the HNT, HNT-NH$_2$, and HNT−NH$_2$−PPy. It is observed that the spherical surface morphology of HNTs, is altered from smooth to rough tubes upon modifications with PPy, moreover based on TEM results, the used HNT present an inner diameter, an outer diameter, and a length in the range of 40, 70, and 500 nm, respectively, we noted as well an increase in the outer diameter upon modification. It also shows that PPy and silver nanoparticles were on the HNTs' surfaces and wrapped inside the tubes [36]. Moreover, Fig. 2h shows the chemical composition of HNT−NH$_2$−PPy material, deduced from EDX; the carbon content was equal to 17%, and Ag NPs were around 2.3%.

The surface composition of the as-prepared materials was deduced from the XPS Analysis, and survey spectra for the HNT and HNT−NH$_2$−PPy samples are presented in Fig. 3a. The surface chemical composition of HNT and HNT−NH$_2$−PPy materials was reported in Table 1. Carbon and nitrogen are present in the chemical composition of the halloysite nano clay and the silane-coupling agent. The silver nanoparticles are from the photosensitizer. Furthermore, Fig. 3b shows the peaks at ~367.13 eV and 373.82 eV attributed to Ag3d5/2 and Ag3d3/2, approving that the metallic state of silver formed upon polymerization [37]. The N1s of HNT−NH$_2$−PPy shown in Fig. 2c are fitted in two components; the free amine (~399 eV) and the quaternized amine at around (~401 eV) [37]. The C1s region (Fig. 3c) shows an inflection point because of the addition of the beta-carbon atom type from polypyrrole, as previously confirmed [38]. A significant increase was noted in C, N, and Ag contents after the polymerization process, and all XPS results confirm the used process's success.

It is worthy to note that in the present work, we have used the AgNO$_3$ as a photosensitizer, to initiate the photo-polymerisation of pyrrole. After the complete reaction, the final product was washed four times with deionized water and ethanol in order to remove the excess of reactants, however after performing XPS and EDX analysis, we have observed another important aspect of this work, is the naturally occurring silver nanoparticles generated from the photosensitizer, through the photopolymerisation. Polypyrrole and silver nanoparticles are generated simultaneously in the form of a composite coating on dispersed, HNTs surfaces, which is of upmost importance, in corrosion protection [39].

3.1.2. Thermal properties of HNT

The Thermogravimetric analysis (Fig. 4), was performed from room temperature to 750 °C under air and at a heating rate of 10 °C/min to check the thermal decomposition of the HNT, HNT-NH$_2$, and HNT−NH$_2$−PPy nanocomposite. Its normalization curves can be found in Fig. S1. For all samples, it revealed two-step thermal degradation. At lower temperatures (less than 100 °C), the weight loss might be due to the removal of moisture and solvent in the different samples, and
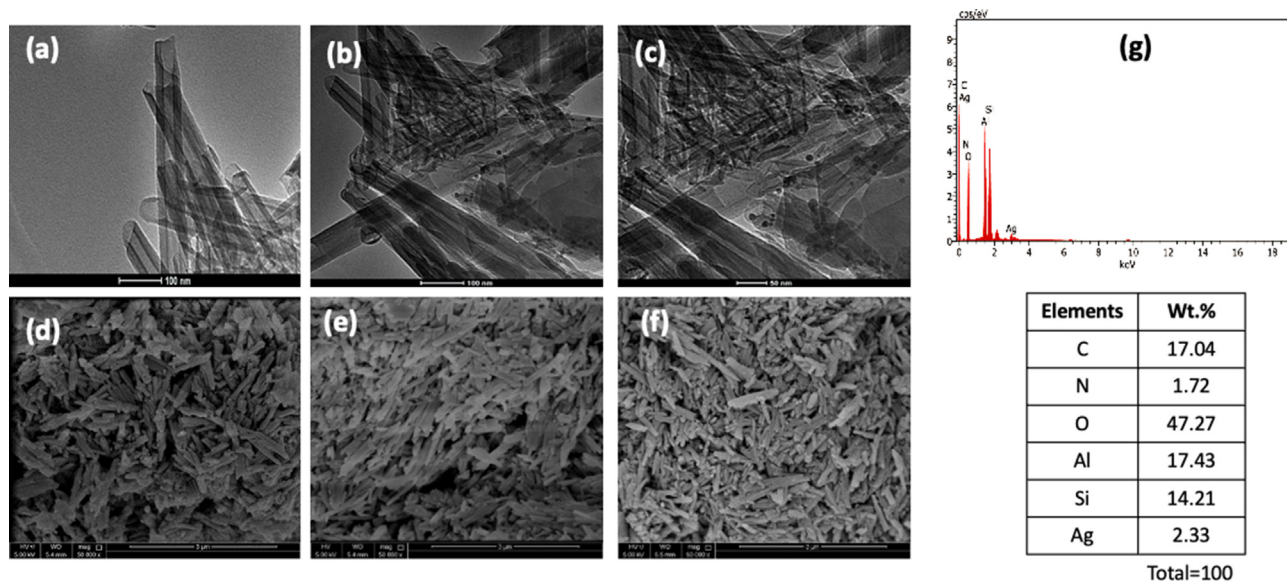
Elements	Wt.%
C	17.04
N	1.72
O	47.27
Al	17.43
Si	14.21
Ag	2.33
	Total=100

Fig. 2 — (a, b, and c) TEM and (d, e, and f) SEM images of HNT, HNT-NH$_2$, and HNT—NH$_2$—PPy nanocomposites, respectively. (g) EDX composition of the composite (HNT—NH$_2$—PPy).

at higher than 489 °C, the thermal degradation is facilitated due to the removal of HNT interlayer-trapped water molecules [40]. As shown in Fig. 4, the used HNT is thermally stable up to 486°, with (only 8% weight loss), which is attributed to the dehydration process due to the removal of interlayer water, for HNT-NH$_2$, and HNT—NH$_2$—PPy samples. The weight loss
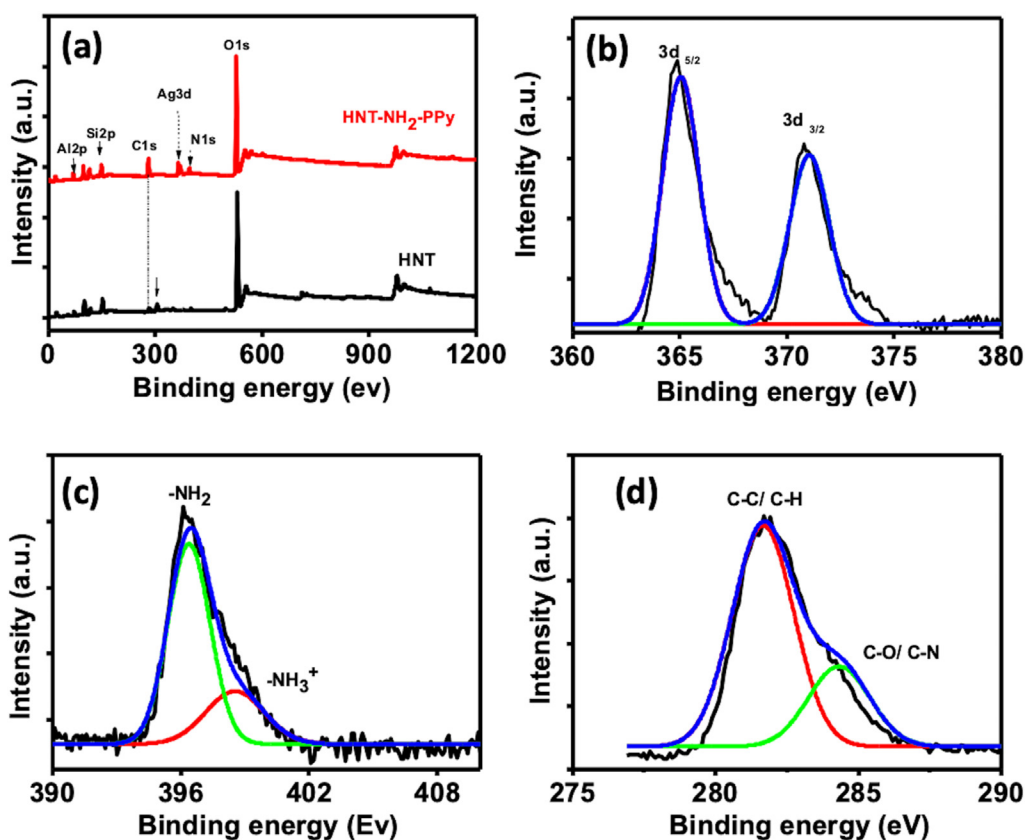

Fig. 3 — XPS spectra of the reference and modified Halloysite, (a) Survey regions of HNT and HNT—NH$_2$—PPy, (b) Ag 3d, (c) N1s, and (d) C1s regions for modified Halloysite.

Table 1 – The atomic percentage from the surface chemical composition, determined from XPS, for HNT-NH$_2$@Ag materials.

Materials	Si	Al	O	C[a]	N	Ag	Na	K	Ca
HNT	16.5	7.90	62.3	2.10	—	—	2.80	0.11	0.50
HNT-NH$_2$-PPy	14.2	17.4	45.2	18.0	2.28	2.30	traces	0.30	0.30

[a] Note that HNTs pristine shouldn't contain carbon; however, the presence of a small amount of carbon (2w%), probably comes from hydrocarbon contamination.

observed between (498 °C—750 °C) is most probably due to the dehydroxylation of HNT and the thermal degradation of both NH$_2$ from silane and PPy polymer chain [41], and from the weight loss of the samples, determined at the end of TGA at 750 °C. The NH$_2$ content was estimated to be 1.4 wt % and NH$_2$-PPy content was estimated to be approximately 2 wt % in HNT-NH$_2$ and HNT—NH$_2$—PPy nanocomposite, respectively. HNT clay was first modified using an NH$_2$ coupling agent, and the PPy conductive polymer chain was modified in the second stage. It was found that it slightly improved the thermal stability (the tg slightly shifted toward the higher temperatures) as compared to the neat HNT (from 489 °C to 500 °C; for HNT—NH$_2$—PPy) due to the interfacial interaction [42], mainly between HNT clay and the amino silane coupling agent, serving as a cross-linking agent. Indeed, the NH$_2$ groups from silane react through a condensation reaction with the free hydroxyl functional groups of HNT, ensuring covalent attachment to the clay sheets [43], and serving as a macro-platform for the PPy polymer chains grafting [44]. Generally, better interfacial interaction bonding imparts better properties to clay polymer nanocomposites, such as tensile strength, hardness, high modulus, and anti-corrosion properties [45].

3.2. Coating characterization

3.2.1. SEM and EDX

The as-prepared and heat-treated NiP, blank NiP/HNT nanocomposite coatings, and their modified ones (NiP/HNT-NH$_2$ and NiP/HNT—NH$_2$—PPy) are exposed to SEM and EDX examination (Figs. 5—7). Generally, the NiP coatings convey a glossy silvery whitish look, whereas their composites offer a slightly blurred silvery physical appearance for the naked eye after removing them from the deposition bath. Fig. 5 clarifies the
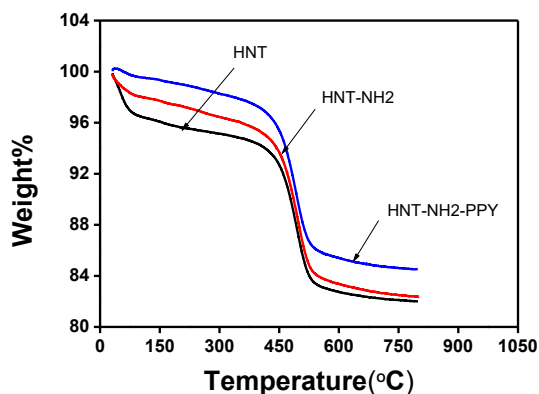

Fig. 4 – TGA thermogram of the bare HNTs and the developed ones (HNT-NH$_2$ and HNT—NH$_2$—PPy).

microscopic studies of the NiP coatings, which characterize a cauliflower-like feature consisting of granules or grains that include fine nodules. These nodules become more and larger upon heat treatment, as shown in Fig. 5b. Growing the circular nodules in the NiP coating indicates the rising deposition of the nickel in the coating matrix, which is proved by the EDX measurements shown in Fig. 5 (c and d). This indicates that the as-prepared NiP coating has an amorphous structure, whereas the heat-treated NiP coating moves to be less amorphous (semi-crystalline) structure, as shown in Fig. 5 (c and d) since the high percentage of the P (>10 wt%) in the coating refers to amorphous structures and less than 5 wt% notifies the pure crystalline structure.

Fig. 5 displays the SEM photos of the NiP/HNT nanocomposite coating, its modified ones, and its EDX mapping. Compared to NiP coating, the changes in the surface morphologies are due to the existence of HNTs and their modifications with NH$_2$ and PPy in the NiP matrix. All nanocomposite coatings shown in Fig. 6 (a, b, and c) have finer-grained nodules close to each other, giving a compact and homogeneous structure compared to the NiP coating. In addition, Fig. 5 (b and c) showed a slightly rougher surface compared to Fig. 5a, which is expected due to the presence of NH$_2$ and NH$_2$-PPy attached to the HNTs after their modification leads to an increase in the branching of HNTs. Furthermore, it is noted that the NiP/HNT-NH$_2$ has a slightly wrinkled shape, whereas the NiP/HNT—NH$_2$—PPy has some medium standalone nodules. The successful deposition of the HNTs and their modifications in the NiP matrix can be clearly shown in the representative Fig. 6a', which is the magnification of Fig. 6a. Fig. 6a', also demonstrated that the diameter of halloysite nanotubes ranges around 60 nm, which is consistent with the TEM results of the HNT diameter, before deposition and embedding in the NiP matrix. For more representation, EDX mapping for the NiP/HNT surface and each element separately is done, as shown in Fig. 5c and d, respectively, which reflects the homogeneous and even distribution of HNT in the metallic matrix surface. The representation of Si, Al, and O proves the presence of HNT, and the representation of Ni and P proves the presence of the NiP matrix and are shown by blue, red, purple, yellow, and green, respectively.

In addition, the prosperous penetration of the HNTs and their modifications particles through the core of the NiP matrix and their good adhesion to the substrate can be confirmed by the SEM/EDX mapping of the cross-sectional specimen of the as-prepared NiP/HNTs as a representative photo, as shown in Fig. 7. The distribution of each element of the composite coating proves their homogeneity inside the NiP matrix. It is revealed that the thickness of the HNT composite coating is approximately 11 μm, which agrees with several
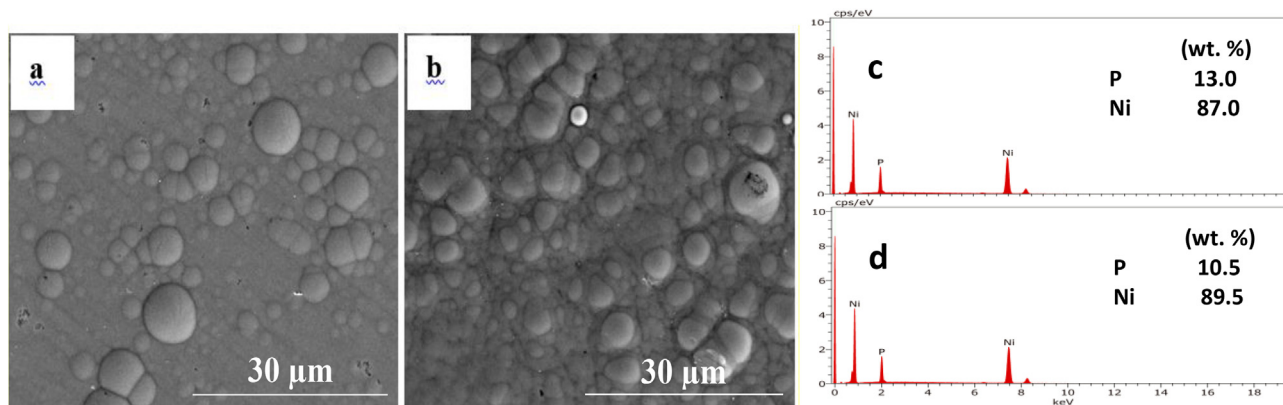
Fig. 5 — SEM images and EDX measurements, respectively, for a, c) as plated and b, d) heat-treated NiP coatings.
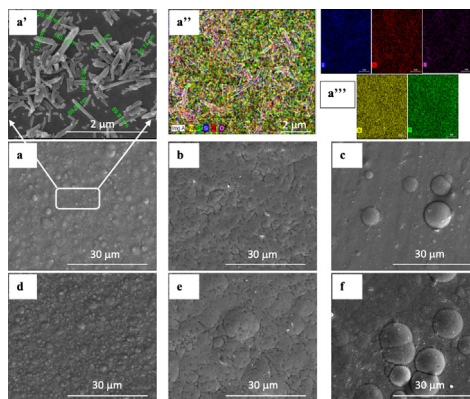

Fig. 6 — SEM images for a, b, and c) as-plated and the corresponding d, e, and f) heat-treated NiP/HNT, NiP/HNT-NH$_2$, and NiP/ HNT−NH$_2$−PPy nanocomposite coatings. a) SEM image of NiP/HNT at higher magnification, a″) EDX mapping of the NiP/HNT at higher magnification, and a‴) The EDX mapping of each HNT and NiP matrix element shows as Al in red, Si in blue, O in purple, Ni in yellow and P in green.

studies in the literature [46,47]. It is worth mentioning that no cracks, pores, voids, or defects were observed at the interface between the nanocomposite coating and the substrate illustrating the superior adhesion of the nanocomposite coatings.

In contrast to the as-prepared nanocomposite coatings, the corresponding heat-treated ones have detectible differences in morphology. They have more significant nodule sizes and rougher surfaces. However, a closer look at the heat-treated nanocomposite coatings' surface topography revealed that their compactness was maintained because of the much dense and closer nodules to each other. Moreover, both modified HNTs coatings (NiP/HNT-NH$_2$ and NiP/HNT−NH$_2$−PPy) offered fewer compactness structures after heat treatment than the blank one (NiP/HNT), especially NiP/HNT-NH$_2$ coating that became more wrinkled structure.

Fig. 8 depicts the EDX measurements for the as prepared and the corresponding heat-treated NiP/HNT, NiP/HNT-NH$_2$, and NiP/HNT−NH$_2$−PPy nanocomposite coatings. The successful incorporation of HNTs and their modification particles in the NiP matrix before and after heat treatment is

demonstrated, as clarified in Fig. 8. In general, the amount of P in the electroless coatings plays a vital role in the power of their properties [48]. It is seen from Fig. 8 that the insertion of either HNTs or their modification particles in the electroless NiP bath causes a reduction in the P content in the composite coatings as compared to the plain NiP coating (Fig. 5). For example, the P content in the as-prepared NiP coating is 13 wt %, which decreases to 11.6 wt % in the as-prepared NiP/HNT coating. The HNT-NH$_2$ and HNT−NH$_2$−PPy particles further reduce the P content to 10.9 and 9.99 wt %, respectively, in their composites. Further reduction is observed in the P content of the heat-treated composite coatings compared to the plain NiP coating and their corresponding as-prepared ones. The most significant reduction occurs in the heat-treated HNT−NH$_2$−PPy, reaching a minimum of 7.11 wt %, which is approximately a 32% and a 29% decrease compared to the heat-treated plain NiP coating and its corresponding as-prepared one, respectively.

As mentioned in the previous SEM section, the decrease in the Ni deposition in the NiP coating leads to a decrease in the
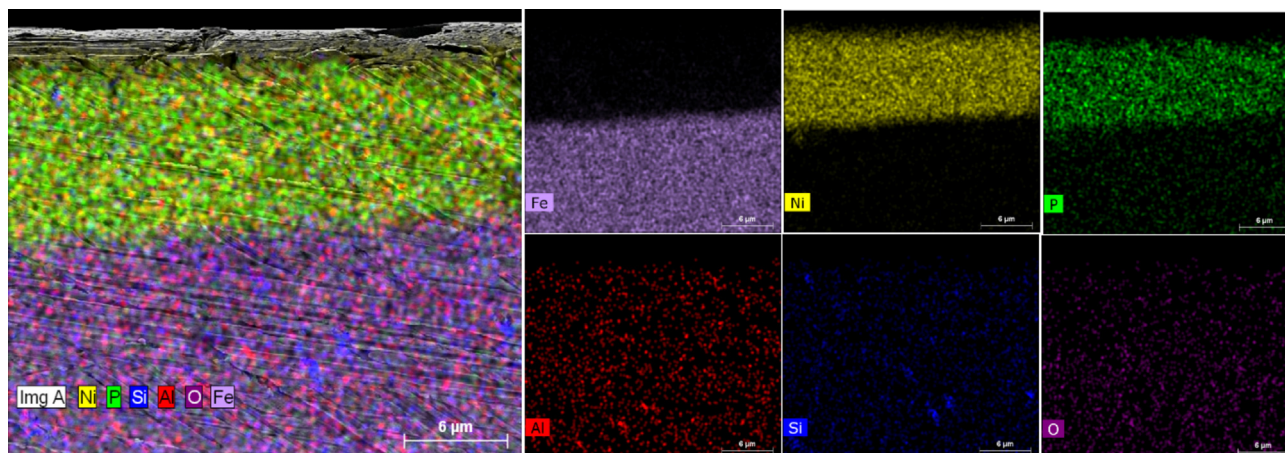
Fig. 7 – Representative SEM/EDX mapping for the cross-sectional image for the as-plated NiP/HNT and distribution of each element present in the composite coating separately, such as; Fe in light purple, Ni in yellow, P in green, Al in red, Si in blue and O in dark purple.

number of the coatings' nodules. Moreover, it is observed that the weight percentage of the Ni is decreased upon the inclusion of HNTs or their modification in the NiP matrix. This means that the EDX results are consistent with the SEM results. For instance, the heat-treated composite coatings have a higher Ni wt. % than the corresponding as-prepared ones, consistent with the increased nodules in the composite coating after heat treatment.

Several factors impact the incorporation of the second phase materials in the electroless NiP matrix comprising the size, charge, inertness, concentration, type of particles, degree, and technique of the bath agitation, and the particles' compatibility with the matrix [48]. Therefore, it is found that the modification of the HNTs particles plays an essential role in influencing its incorporation level. The modified HNT with NH_2 minimizes the Al and Si, representing the HNT incorporation content in the NiP matrix of about 50%, as shown in Fig. 8b. Further modification of the HNTs with NH_2-PPy leads to a further decrease in the wt. % of both Al and Si. This is due to an increase in the branching of the HNTs particles, causing an increase in the mean distance between them, resulting in a further decrease in its level of incorporation.

3.2.2. Roughness and hydrophobicity

The topological features and the hydrophobicity of the as-prepared and heat-treated NiP and its composites with blank HNTs (NiP/HNT) and their modification with NH_2 (NiP/HNT-NH_2) and NH_2-PPy (NiP/HNT–NH_2–PPy) coatings are analyzed using AFM and contact angle measurements, respectively. Fig. 9 shows 3D images and the roughness profiles (R_a) of the different nanocomposite coatings before and after heat treatment. It can be noticed that adding the HNTs and derivate materials, as well as the heat treatment of the coatings has an effect on the surface profile, topography, and roughness of the NiP coating, as seen in Fig. 9. The as-prepared NiP coatings generally have the smoothest surface, which moved to contain tiny hills and valleys by adding the HNT. Fig. 9 (AFM

characterization) clarified the nodular structure of the NiP surface and presence influence of HNTs and their modification particles on the homogeneity of the NiP coating. In addition, the quantitative analysis results show an increasing trend in average surface roughness (R_a) of NiP coating from 4.72 nm to 6.85 nm after adding HNT, leading to a 1.45 times surface roughness improvement. Furthermore, about 1.26 and 1.98 times enhancement in the roughness of the HNT composite coating after its modification with NH_2 and NH_2-PPy, respectively, are noticed. The rise in surface roughness can be attributed to the increased branching of the modified HNT with NH_2 or NH_2-PPy, which obstructs the smooth movement of the AFM cantilever probe tip across the coated surfaces, creating a barrier. This parallel with previous research in literature [49–56] confirms that the addition of the second particles to the NiP matrix results in an increase in surface roughness. Commonly, the degree of roughness alteration resulting from the addition of second particles is reliant on a number of factors, including particle type, size, volume concentration, and coating thickness [57]. Xiang et al. [58] propose that by introducing nanoscale diamond particles (0.52–2.21 wt %) into the electroless Ni–P matrix, the surface transforms from a smooth, shiny appearance to a hazy, rough surface with nodular protrusions spreading across the whole surface. A quantitative comparison with previous work can be found in Table S1 [49–56].

The probable reason for the increased Ra roughness after annealing is that annealing treatments offer the atoms enough activation energy to diffuse to the site with the lower surface energy in the horizontal direction. The atoms' rearrangement leads to a rougher surface and an increase in the grain size of the composite coatings [59,60]. That is why, the heat-treated composite coatings offered further increments of about 10, 20, 30, 40, and 50% in their roughness compared to their corresponding as-prepared ones.

Additionally, it is observed that all coatings indicated a hydrophobic nature where their WCA is higher than 90, except
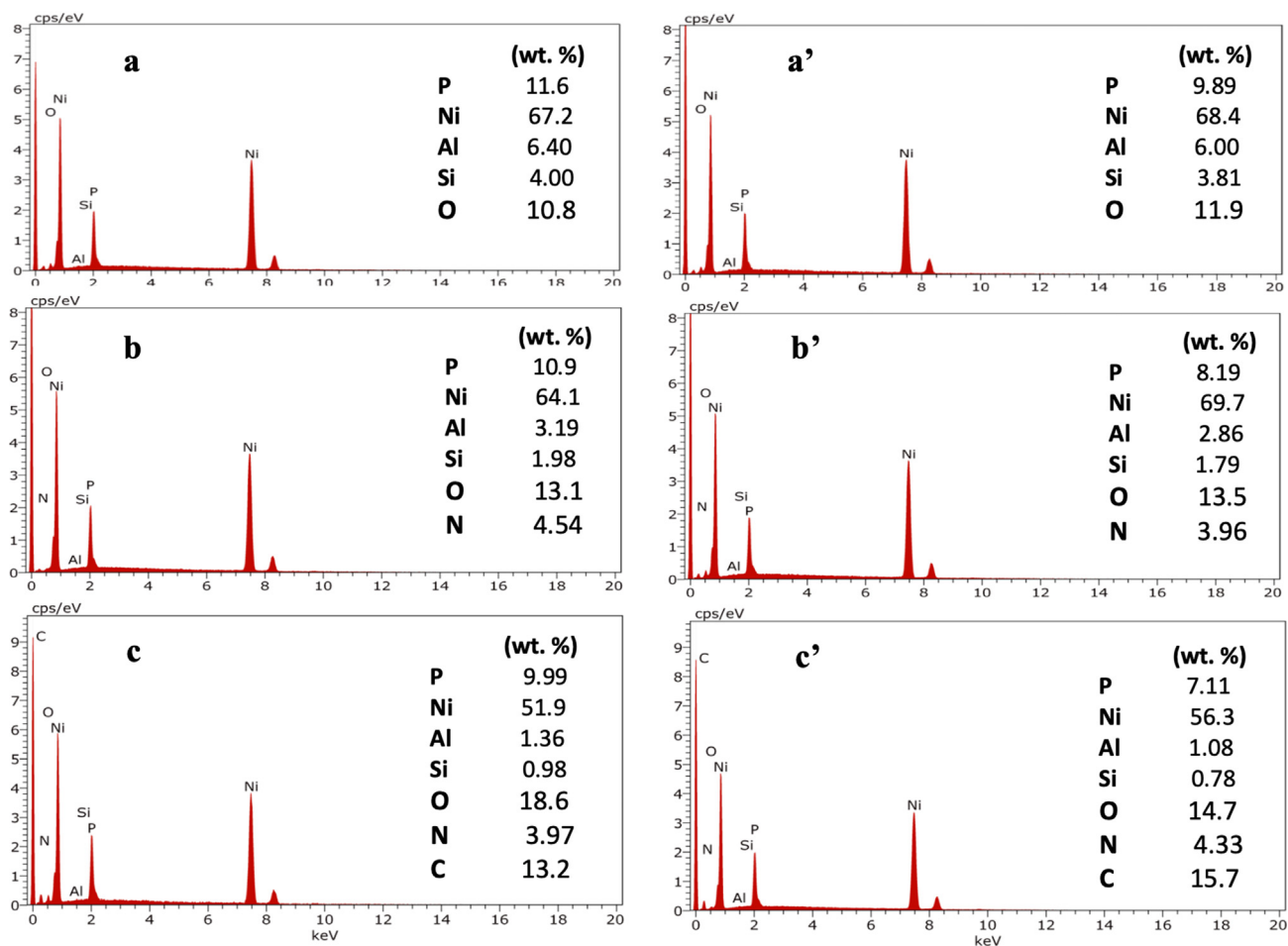
Fig. 8 − EDX measurements for a, b, and c) as-prepared and the corresponding a, b, and c; heat-treated NiP/HNT, NiP/HNT-NH$_2$, and NiP/HNT−NH$_2$−PPy nanocomposite coatings.

the heat-treated plain NiP, which shows a hydrophilic nature where it has a WCA of around $87 \pm 1°$; this is due to the formation of the nanocrystalline structure after Ni recrystallization that leads to change in the surface chemistry. The hydrophobicity of all composite coatings is higher than that of the plain NiP coatings, as the water contact angles (WCAs) of the coatings are mentioned in Fig. 9. In contrast, there is no change in the hydrophobicity of the blank NiP/HNT nanocomposite coatings and their composites after modifications (NiP/HNT-NH$_2$ and NiP/HNT−NH$_2$−PPy) before or after heat treatment. The hydrophobicity of the plain NiP coating is about $105 \pm 1°$ whereas those of the composite coatings before and after heat treatment are around $110 \pm 1°$. This is due to the presence of the pristine and modified HNTs in the NiP matrix, enhancing the composite coatings' compactness.

3.2.3. XRD

Fig. 10 shows the XRD patterns of HNTs and their modifications, as-prepared and heat-treated NiP, NiP/HNT, NiP/HNT-NH$_2$, and NiP/HNT−NH$_2$−PPy nanocomposite coatings. The face-centered cubic structure of the Ni (111) plane is indicated by a predominated broad peak at 2θ of 44.5° in the XRD spectra

of the as-prepared NiP coating displaying an amorphous structure [60]. This is due to alloying the nanocrystalline Ni with high P in the deposition process resulting in the distortion of the Ni lattice. Noticeably, all as-prepared HNTs composite coatings have an analogous peak at the same position, as shown in Fig. 10a, without any recognition peaks appearance fo either the pristine or the modified HNTs. The disappearance of the pure and modified HNTs could be attributed to their fine size and their small amount that is deposited in the NiP coating, as seen in EDX results, and due to the high Ni diffraction peaks density as well. In addition, the similar structures of all HNTs composite coatings with the plain one confirm the non-influence of our added materials on the crystallization process of the NiP coating. It is noteworthy to mention that there is an obvious difference between the values of the full width at half−maximum (FWHM), which is acquired from the XRD pattern, of the plain NiP and the HNTs composite coatings, such as the FWHM of the plain coating which is 0.5110, whereas that one of the NiP/HNT coating which is 0.1535. This proves the refinement of the NiP nodules and the boosting of the crystalline phase formation due to the presence of the HNTs in the NiP matrix. However, the
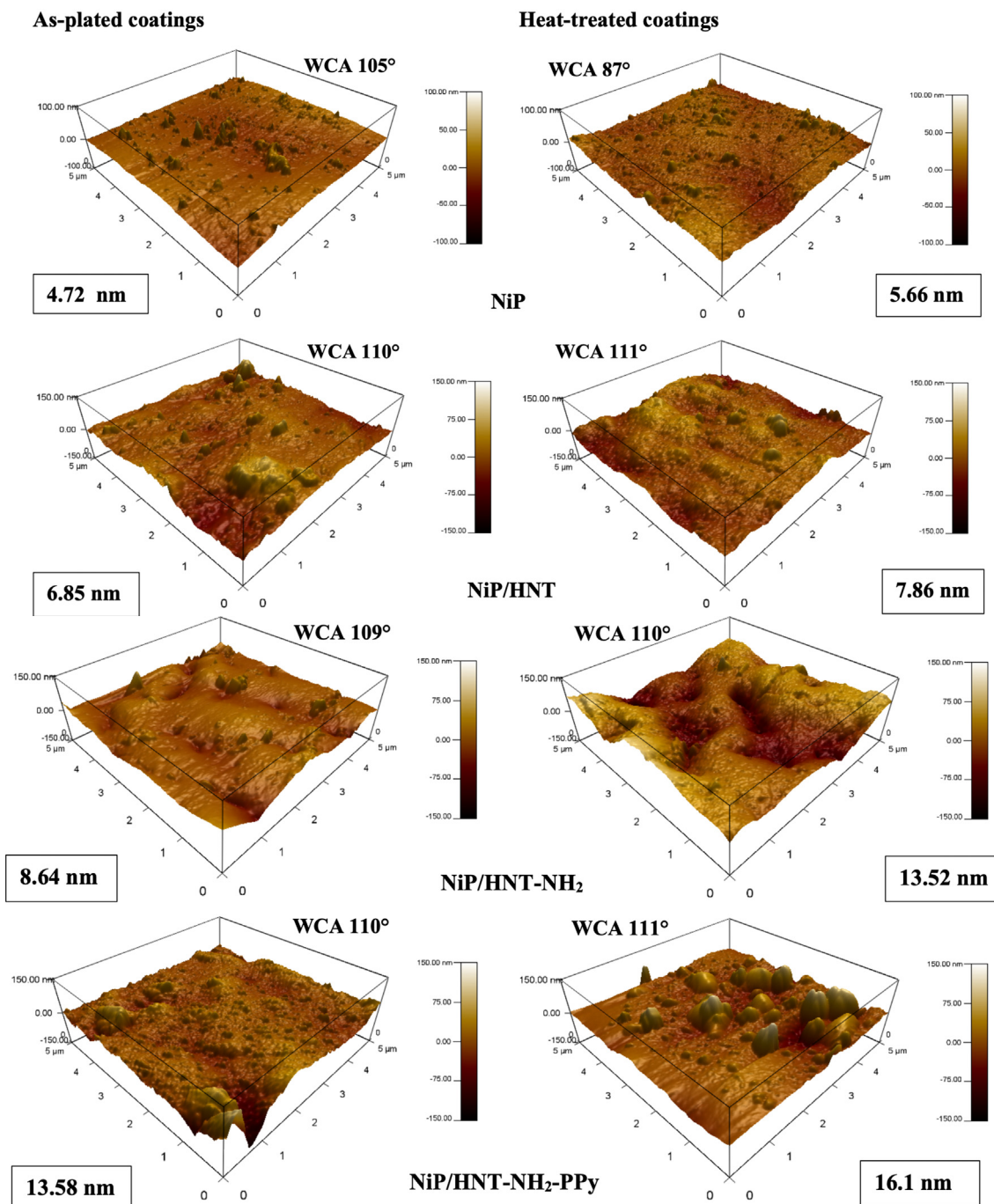
As-plated coatings   **Heat-treated coatings**

Fig. 9 – 3D-AFM topographic images along with respective surface-roughness profiles of NiP, NiP/HNT, NiP/HNT-NH$_2$, NiP/HNT–NH$_2$–PPy coatings before and after heat treatment. The water contact angle (WCA) values of all coatings are mentioned.

modification of the blank HNTs with NH$_2$ and NH$_2$-PPy slightly increases the FWHM values of their composite coatings, as they are 0.2047 and 0.2093, respectively.

Fig. 10b shows the XRD peaks of all coatings after heat treatment. The crystalline diffraction peaks corresponding to the Ni and Ni$_3$P phases are noticed in the NiP coating, clarifying the transformation of its amorphous structure before

annealing to become a crystalline one, which is in line with several literature research types [61,62]. Similarly, all heat-treated HNTs composite coatings have identical XRD patterns to those of the plain heat-treated NiP coating, reflecting that the pristine and modified HNTs do not influence the peak positions of the NiP coatings. However, they slightly change the intensities of the Ni and Ni$_3$P peaks.
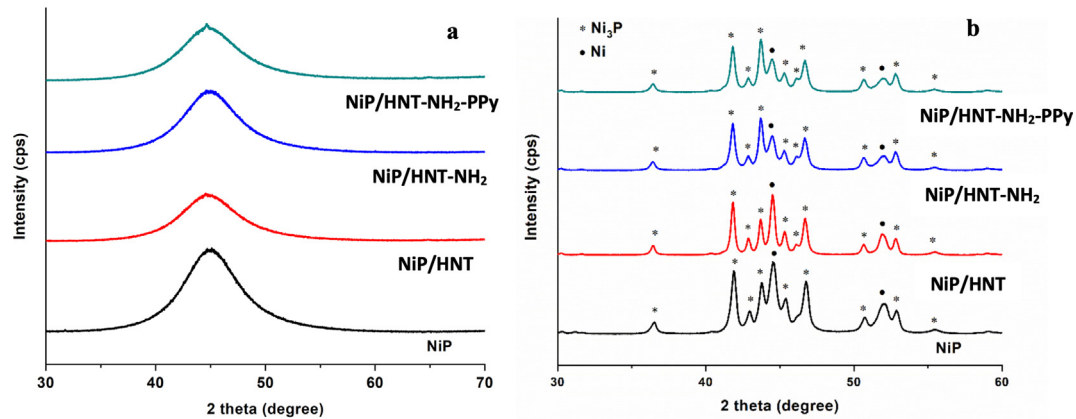
Fig. 10 – XRD pattern for NiP, NiP/HNT, NiP/HNT-NH$_2$, NiP/HNT–NH$_2$–PPy coatings before (a) and after (b) heat treatment at 400 °C for 1 h.

3.2.4. Microhardness

Vickers hardness and Nanoindentation techniques were utilized to assess the mechanical strength and the hardness characteristics of all as-prepared and heat-treated nanocomposite coatings, compared with the corresponding plain one before and after heat treatment. The results are exhibited in Fig. 11 and Table 2.

Fig. 11a depicts the Vickers microhardness outcomes of the as prepared and heat-treated NiP and NiP/HNT, NiP/HNT-NH$_2$, and NiP/HNT–NH$_2$–PPy nanocomposite coatings. It is noteworthy that the NiP coating has a microhardness of about 490 HV$_{200}$, which is increased by about 12% with the production of NiP/HNT nanocomposite coating, as seen in Table 2. The nanocomposite coatings of NiP/HNT-NH$_2$ and NiP/HNT–NH$_2$––PPy offered about 22.5 and 18.5%, further increase in the microhardness of the plain NiP coating, respectively. Moreover, it is clarified that the further modification of the HNT-NH$_2$ with PPy caused a slight reduction in the microhardness of its composite coating (NiP/HNT–NH$_2$–PPy) compared to the one that is modified with NH$_2$ only (NiP/HNT-NH$_2$). This is attributed to the extra branching of the modified HNTs with NH$_2$-PPy, which slightly weakens the hardness effect of NH$_2$, which acts as a hardener that causes, to some extent, the enhancement of the cross-linking of the material. Therefore, the NiP/HNT-NH$_2$ nanocomposite coating has the highest microhardness.

Generally, the enhancement of the microhardness of the HNT nanocomposites coatings can be explained based on the strengthening mechanism of alloys and polycrystalline metals [63], which is described on the grain refinement from Hall-Patch relationship, solid solution strengthening, crystal orientation, and dispersion strengthening. Therefore, the uniform distribution of the HNTs and their modifications particles in the NiP matrix, as seen in the SEM/EDX mapping (Fig. 7), can suppress the grain growth of the NiP alloy and refine them, resulting in the reduction of the plastic deformation of the matrix under loading. On the other hand, a grain refiner can function as a heterogeneous nucleation site during solidification through the grain refining process [64]. Hence, dispersed HNT in the deposition bath can provide many heterogeneous nucleation sites, thereby enhancing the nucleation rate, preventing the lateral growth of grains, and forming fine-grained structures. The following equations (Eqs. (1) and (2)) are the Hall-Petch equations [65] that describe grain refinement strengthening.

$$\sigma_y = \sigma_0 + kd^{-1/2} \tag{1}$$

$$HV \approx 3\sigma_y \tag{2}$$

where σ_y Is the yield stress, σ_0 is the material stress constant required to start dislocation motion, k is a constant, d is grain diameter, and H.V. is microhardness.

The heat treatment causes an extra enhancement in the microhardness of the NiP coating and the HNTs nanocomposite ones, as shown in Fig. 11a and Table 2. About 260 HV$_{200}$ increase in the microhardness of the heat-treated NiP coating compared to its corresponding one before heat treatment. Similarly, the heat-treated NiP/HNT, NiP/HNT-NH$_2$, NiP/HNT–NH$_2$–PPy nanocomposites coatings displayed approximately 49%, 55%, and 50% improvement in their microhardness compared to their corresponding as-plated ones, respectively, as clarified in Table 2. As shown in the XRD results (Fig. 10), the creation of the challenging Ni$_3$P phase in the coatings and the amorphous phase transition to the crystalline one after heat treatment are the essential key factors behind the microhardness upgrading of the heat-treated coatings [66,67]. It is worth mentioning that the trend of reduction and enhancement in the microhardness of the heat-treated coatings is similar to the corresponding as-plated ones.

This technique is utilized to measure the nanomechanical properties of the coatings in the submicron range with nanometer resolution [68]. The nanoindentation test for the plain NiP coating and the different HNTs nanocomposite coatings, before and after heat treatment, is done, and the outcomes are represented in Fig. 11b, which displays the relationship between the loads and the penetration depths. The penetration depths reflect the hardness of the coatings; therefore, the increase in the hardness of the coating reduces its penetration depth.
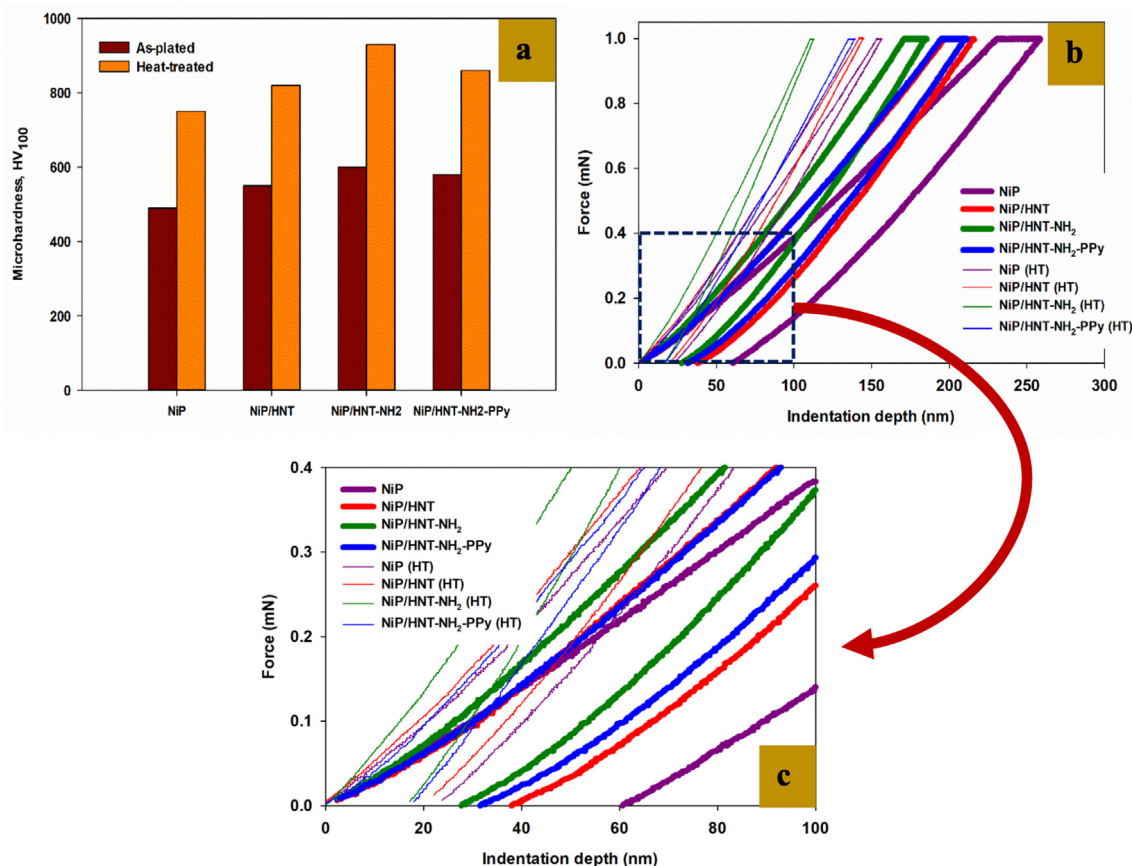
Fig. 11 — Mechanical properties of NiP, NiP/HNT, NiP/HNT-NH$_2$, and NiP/HNT—NH$_2$—PPy nanocomposites coatings before and after heat treatment (a) Vickers microhardness, (b) nanoindentation load-displacement curves and (c) the magnification of the marked area in (b).

Fig. 11c shows the magnification of the marked area in Fig. 11b to clarify the differences in the indentation depths for the various coatings. It is observed that the as-prepared plain NiP coating has the most significant penetration depth, around 60 nm, and has a minor hardness (4.94 GPa). By the insertion of the pristine and (NHT-NH$_2$ and NHT—NH$_2$—PPy) in the NiP matrix, the indentation depth of the plain coating is reduced approximately 22, 32 and 29 nm, respectively, as shown in Fig. 11c, and their hardness is increased. The smaller displacements indicate the higher resistances offered by the HNTs nanocomposite coatings to the indenter, as illustrated in Table 2. Furthermore, a higher decrease is noticed in the

indentation depths of the heat-treated coatings, in contrast to their corresponding as-prepared ones, confirming their higher hardness. Moreover, the heat-treated NiP/HNT-NH$_2$ nanocomposite coating has the lowest penetration depth, which is about 40.5% and 32.7% less compared to its corresponding as-prepared coating and the heat-treated plain NiP one, respectively, as shown in Fig. 11c. This is attributed to the modification of HNT with NH$_2$, which acts as a hardener, leading to better cross-links in the composite and enhancing its microhardness composite coating.

Generally, the effects of grain refinement and dispersion hardening, as previously mentioned, in addition to the formation of composite structures, are the main reasons for the development of the coating hardness [69—71]. The role effect of the composite structure formation in enhancing the HNTs nanocomposite coatings can be calculated using the below Eq. (3) related to the mixture law [71].

$$E_c = E_m V_m + E_p V_P \tag{3}$$

where E represents the hardness value, V is for the volume fraction, c mentions for composite, m mentions for matrix, and p mentions nanoparticles.

Finally, it is worth mentioning that the increasing and decreasing trend in the microhardness values of the different coatings obtained from the Nano-indentation technique

Table 2 — Vicker's microhardness and hardness values obtained from the Nanoindentation test of the different coatings before and after heat treatment at 400 °C for 1 h.

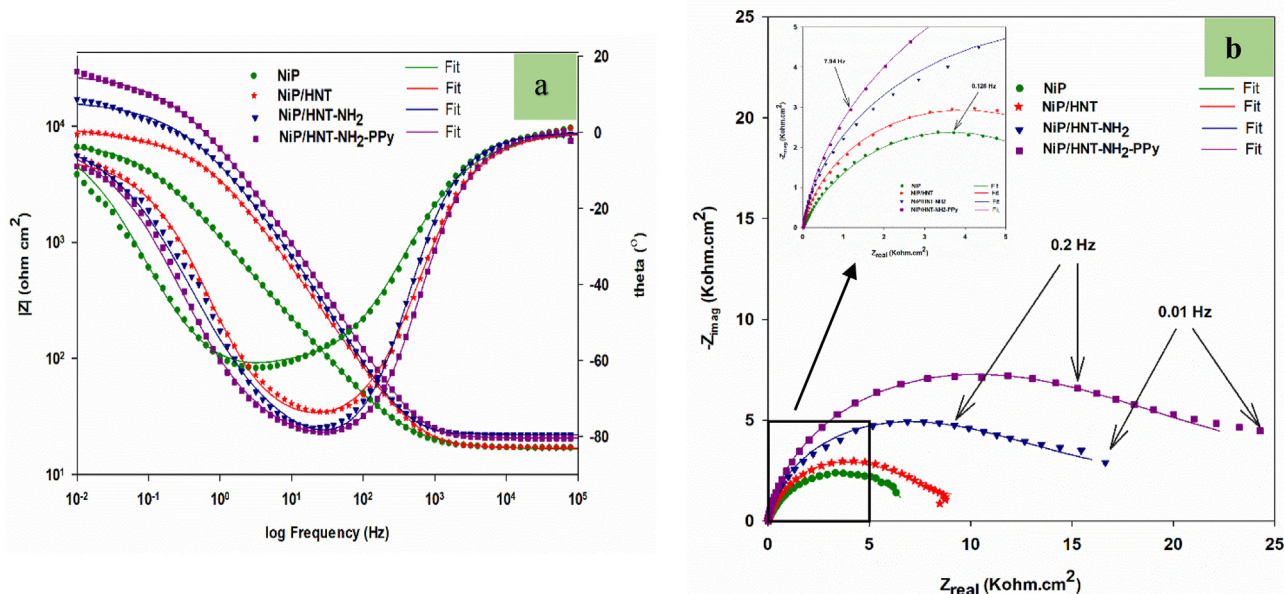| Coating's name	Vickers microhardness (HV$_{200}$)		Nanoindentation hardness (GPa)	
	Before HT	After HT	Before HT	After HT
NiP	490	750	4.94	6.95
NiP/HNT	550	820	5.98	7.17
NiP/HNT-NH$_2$	600	930	6.12	11.2
NiP/HNT—NH$_2$—PPy	580	870	5.61	8.14

Fig. 12 – (a) Bode/phase angle and (b) Nyquist plots of the different as–prepared NiP nanocomposite coatings immersed in 3.5 wt % NaCl solution at room temperature.

coincides with those obtained from Vickers microhardness, as shown in Table 2.

3.2.5. Electrochemical properties

Electrochemical impedance spectroscopy (EIS) and potentiodynamic polarization electrochemical techniques are applied at room temperature to illustrate the anticorrosion properties of the plain NiP coating and the HNTs nanocomposite coatings. A 3.5 wt% NaCl solution was utilized when recording the electrochemical behavior and the corrosion protection enhancement influence of the HNTs and their modification (HNT-NH$_2$ and HNT–NH$_2$–PPy) on the NiP coating.

3.2.5.1. *Electrochemical impedance spectroscopy (EIS)*. Fig. 12 displays the EIS results in Bode-phase angle and Nyquist plot formats obtained under static conditions and at open circuit potential (OCP) for different nanocomposite coatings (NiP/HNT, NiP/HNT-NH$_2$, and NiP/HNT–NH$_2$–PPy), as well as NiP as a control sample.

In Bode plots, at low frequencies ($|Z_{0.01}$ Hz$|$), the higher the absolute impedance value for the inspected sample, the greater its corrosion resistance [72,73]. As shown in Fig. 12a, the as-prepared NiP coating has the lowest absolute impedance value compared to the other composite coatings. Upon incorporation of HNTs in the NiP matrix, the absolute impedance value of the NiP/HNT nanocomposite coating has increased compared to that of the HNT-free coating. Furthermore, it is noticed that the modification of HNTs with either NH$_2$ or NH$_2$-PPy greatly enhances the absolute impedance value of both modified nanocomposite coatings (NiP/HNT-NH$_2$ and NiP/HNT–NH$_2$–PPy), where the highest absolute impedance value is obtained for the HNT nanocomposite coating that is further modified with PPy (NiP/HNT–NH$_2$–PPy).

In general, the protective behavior of the NiP coating is due to the interaction of the water with the present phosphorous in the matrix, producing a hypophosphite layer that passivates the nickel and keeps it from hydration in the corrosive solution [74]. However, the improvement in the absolute impedance values for the unmodified and modified HNT nanocomposite coatings is mainly attributed to the protective strength of the HNTs and their modification particles, in addition to their excellent distribution in the NiP matrix. Moreover, the good compactness and well adhesion of the HNT nanocomposite coating on the substrate, as previously described in SEM results, reduce the active sites for the diffusion of the electrolyte and corrosion attacks. Moreover, the further enhancement in the absolute impedance value of the NiP/HNT–NH$_2$–PPy nanocomposite coating is attributed to the popular conducting polymer "polypyrrole," known for its solid protective ability in different corrosive media. In addition, including the Ag atom in the preparation process of the NiP/HNT–NH$_2$–PPy nanocomposite coating offers an extra effect in improving the protective properties of the coating.

Besides, the higher maximal peak values (θ) observed in the phase angle plots of the different HNT-nanocomposites coatings compared to that of the HNT-free coating illustrates their high corrosion protection properties. The NiP/HNT–NH$_2$–PPy nanocomposite coating has the highest (θ) value compared to the other HNT-nanocomposite ones, affirming its superior protection behavior, as shown in Fig. 12a. It is worth mentioning that the different HNT-nanocomposite coatings have phase angle plots with similar shapes indicating that the exact electrochemical corrosion mechanism occurs.

The corresponding Nyquist plots for the as-prepared NiP and un-modified and modified HNT-nanocomposite coatings are shown in Fig. 12b. It is known that the wider the diameter

of the Nyquist semicircle, the larger the inhibitive ability of the coating. It is observed that the Nyquist plots for all different coatings have the same appearance as the depressed semi-circles with different areas under the curves. Accordingly, it can be said that all coatings have the exact corrosion mechanism with different degrees. Comparing the Nyquist curves of all coatings to their bode plots, it is noticed that they have the same enhancement and reduction trend in the protection efficiencies of the coatings. For example, adding HNT increases the size of the semicircle of the HNT-free coating, and the increase is more significant with both modifications of the HNTs. Moreover, further modification of HNT with PPy leads to a further increase in the area under the semicircle curve of its nanocomposite coating. Hence, the modified HNT with both NH_2 and PPy creates a more dense, compact composite coating that isolates the substrate from the electrolyte solution resulting in the largest Nyquist semicircle size with the highest phase angle maxima.

The equivalent circuit shown in Fig. 13 was implemented when the impedance behavior of different coated specimens was modeled using Gamry's Echem Analyst software. As shown in Fig. 12, the matching between fitting and experimental plots reflects the concurrence between the equivalent circuit's model and the actual impedance behavior of the coated samples. The equivalent circuit is shown in Fig. 13 and consists of two-time constants; where the first one contains the solution resistance (R_s), which is connected to the coating capacitance (CPE_{coat}), which is parallel to the pore resistance (R_{po}). The second time constant consists of the charge transfer resistance (R_{ct}) and the double-layer capacitance (CPE_{dl}) to account for the interface between the coated layer and the electrolyte. Appearance of Warburg diffusion element (W) in the circuit is due to the existence of electrolyte diffusion [75]. The presence of the pseudo-capacitive element (CPE) is to standardize the deflection of the surfaces' inhomogeneous, due to the irregularity in the current circulation at the surface or the roughness [76], from the idealistic capacitive performance. The Equation shown below (Eq. (4)) is applied to calculate the impedance value of CPE [77],

$$Z_{CPE} = \frac{1}{Y_0(j\omega)^n} \tag{4}$$

The CPE constant is mentioned by (Y_0). The j, ω, and n, respectively, symbolize the unreal number, the A.C. signal' angular frequency (1/rad), and the CPE exponent. The n value fluctuates from 0 to 1. The CPE exhibits exemplary capacitor behavior if n turns into 1. Furthermore, the double-layer capacitance (C_{dl}) of the coating can be analyzed by following Eq. (5) [78].

$$C_{dl} = \sqrt[n]{\frac{Y_c}{R_{ct}^{(n-1)}}} \tag{5}$$

Y_c signifies the coating' CPE constant, and R_{ct} mentions to the charge transfer resistance. As shown in Fig. 13, the high-frequency time constant is referred to the interface between the coating and the solution and is demonstrated by the grouping of CPE_{coat} and R_{po}. In addition, the grouping of CPE_{dl} and R_{ct} is related to the low-frequency time constant, which reflects the electrochemical reactions at the interface between

the substrate and the coating. The fully fitted and modeled parameters are presented in Table 3.

Table 3 shows that the R_{ct} of the HNT-free coating (NiP) is about 2.3 times less than that of the obtained composite coating after inserting the blank HNTs into the NiP matrix. This indicates the significant protection behaviors of the NiP/HNT nanocomposite coating. Furthermore, the modification of the HNT with either NH_2 or NH_2-PPy leads to a further rise in the R_{ct} value of their composite coatings by about 1.6 and 2.4 times, respectively, compared to that of the blank HNT one. Therefore, the highest protection efficiency (82%) is observed with the NiP/HNT–NH_2–PPy nanocomposite coating. This confirms the uniform distribution of the blank HNTs and their modification particles in the NiP matrix and the excellent adherence of their composites with the substrate.

Similarly, it is noted that the R_{po} (pore resistance) values of the various as-prepared NiP and HNTs nanocomposite coatings have the same enhancing trend as their analogous R_{ct} values. For example, as shown in Table 3, the further modification of HNT with NH_2-PPy raises the R_{po} value of the resulting NiP/HNT–NH_2–PPy nanocomposite coating by about 205 and 226%, respectively, compared to the analogous R_{po} values of the HNT-free coating (NiP) and blank HNT nanocomposite coating (NiP/HNT). In addition, the presence of HNTs or their modification particles in the NiP matrix exhibits lower values of CPE_{dl} than that of the HNT-free coating, as shown in Table 3, signifying the reduction in the interaction between the substrate and the electrolyte. The lowest value of CPE_{dl} of the NiP/HNT–NH_2–PPy coating confirms that this coating extra seals off the voids and instructs greater separation between the substrate and the electrolyte, reflecting its efficient impermeability and ascendant protection capability against corrosion.

On the other hand, Bode/phase angle (a) and Nyquist (b) plots of the heat-treated HNT-free (NiP) and HNTs nanocomposite (NiP/HNT, NiP/HNT-NH_2, and NiP/HNT–NH_2–PPy) coatings are elucidated in Fig. 14. The heat-treated coatings have higher impedance behavior than their analogous as-prepared ones. For example, Nyquist and Bode plots of the heat-treated NiP have a higher absolute impedance value and a larger area under its semicircle than those of the corresponding as-prepared one, as compared in Fig. 12 (a and b) and 14 (a and b), respectively. The heat-treated coatings do not
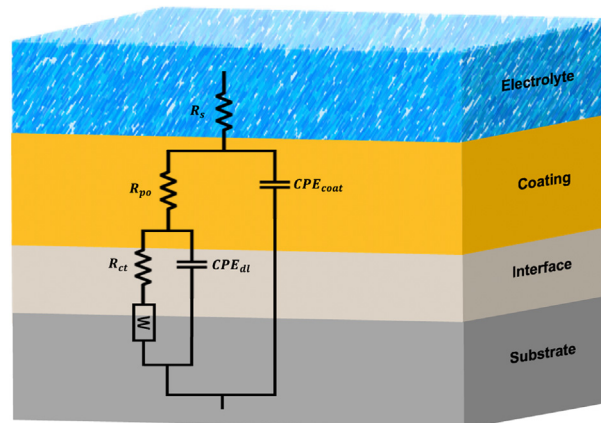

Fig. 13 – Two-time constants equivalent circuit.

Table 3 − EIS fitting results of the different−as prepared NiP nanocomposite coatings immersed in 3.5 wt % NaCl solution at room temperature.

Coating (as-prepared)	Rs ($\Omega \cdot cm^2$)	R_{po} ($\Omega \cdot cm^2$)	CPE_{coat} ($\mu F \cdot cm^{-2} S^{-n}$)	R_{ct} ($\Omega \cdot cm^2$)	CPE_{dl} ($\mu F \cdot cm^{-2} S^{-n}$)	n	I.E. (%)
NiP	17.4	867	179	8600	169	0.76	−
NiP/HNT	16.5	1306	113	19,810	31.7	0.89	56.6
NiP/HNT-NH$_2$	18.9	1780	45	31,950	24.9	0.93	73.1
NiP/HNT−NH$_2$−PPy	21.8	1960	43	47,800	20.5	0.97	82.0

have the same impedance behavior as their corresponding as-prepared ones. Therefore, both heat-treated modified HNT nanocomposite coatings (NiP/HNT-NH$_2$ and NiP/HNT−NH$_2$−PPy) have lower absolute impedance values than the heat-treated blank HNT nanocomposite coating (NiP/HNT).

Consequently, the blank HNT nanocomposite coating has the highest absolute impedance value amongst the other heat-treated coatings. Nevertheless, the heat-treated modified HNT nanocomposite coatings still have higher absolute impedance values than the HNT-free coating, as shown in Fig. 14a. Additionally, the absolute impedance values of the NiP/HNT−NH$_2$−PPy coating are still higher than the NiP/HNT-NH$_2$ coating due to the protective polypyrrole impacts. The less impedance of the modified HNT composite coatings may be due to the slight degradation of the organic part of HNT (NH$_2$ and NH$_2$-PPy) during the heat treatment process, despite their high thermal stability that is previously shown in TGA measurements (Fig. 4). Another reason may be due to the decreased compatibility of both NH$_2$ and NH$_2$-PPy with the crystalline structure of NiP coating obtained after heat treatment, see SEM photos in Fig. 6, which display the decreased compactness of their nanocomposite coatings in comparison to the blank NiP/HNT nanocomposite coating.

Additionally, the changed shape of the phase angle plots of the modified HNT nanocomposite coatings related to the blank HNT and HNT-free ones indicate that they follow a different fundamental electrochemical process. They show a more transparent two-relaxation process, validating the two-time constant's behavior. Moreover, the phase angle plot for the heat-treated NiP/HNT coating has the maximum peak (θ). It is worth mentioning that the corresponding Nyquist plots of various heat-treated coatings showed a similar impedance behavior trend to their corresponding heat-treated Bode plots, as shown in Fig. 14 (a and b). On the other hand, the Nyquist plots of different heat-treated coatings exhibited higher semicircle diameters compared to their corresponding as-prepared ones. The highest semicircle diameter is noted with the NiP/HNT nanocomposite coating, as clarified in Fig. 14b.

Warburg diffusion element (W) is observed in the case of the heat-treated NiP coating. Similarly, the impedance behavior of various heat-treated coatings is fitted following the two-time constants equivalent circuit is shown in Fig. 13. The fitted parameters of the impedance behavior of the different coatings are summarized in Table 4.

As demonstrated in Table 4, the enhancement in the total corrosion resistances (R_{po} and R_{ct}) of the various heat-treated coatings concerning their corresponding as-prepared ones is distinctly noticed. In addition, there is a decrease in the capacitance values (CPE_{coat} and CPE_{dl}) of the different coatings after heat treatment. This indicates the decreased permeability and increased compactness of the heat-treated coatings that impede the electrolyte flow to the substrate. Notably, R_{po} and R_{ct} values of the heat-treated NiP coating are improved by about 3.7 and 3.5 times, respectively, in comparison with those values before heat treatment. The formed dense and less porous structure of NiP coating, due to the formation of new phases after the proper heat treatment as described in the XRD section, is the main reason for the enhancement of its protection ability, as clarified in the literature [79].

Contrary to the as-prepared coatings, the heat-treated NiP/HNT has the highest R_{po} and R_{ct} values, in comparison to the other heat-treated ones, pursued by a reduction in its R_{po} and R_{ct} values, respectively, by about 37.8 and 45%, upon modification of HNT with NH$_2$, and by about 20 and 29.4%, upon further modification of HNT with NH$_2$-PPy, as shown in Table 4. This excellent protection enhancement (89.5% efficiency) of the heat-treated NiP/HNT coating can be related to its outstanding homogeneity and compactness, as previously explained in the SEM section. Further, it is worth mentioning that the R_{po} and R_{ct} values of both heat-treated modified HNT nanocomposite coatings are higher than those of the heat-treated HNT-free coating. NiP/HNT-NH$_2$ and NiP/HNT−NH$_2$−PPy coatings offered a protection efficiency reaching 81 and 85%, respectively, compared to the as-prepared NiP coating.

3.2.5.2. Potentiodynamic polarization measurements (P.P.). Fig. 15 shows Tafel plots of the as-prepared and the corresponding heat-treated NiP, NiP/HNT, NiP/HNT-NH$_2$, and NiP/HNT−NH$_2$−PPy nanocomposite coatings in 3.5 wt % NaCl solution at room temperature. Table 5 outlines the main extracted electrochemical parameters from the Tafel curves, which are the E_{corr} (corrosion potential), the i_{corr} (corrosion current density), and the Tafel slopes (b_c and b_a). In addition, Table 5 includes the corrosion inhibition efficiencies (I.E. %) of the various coatings before and after heat treatment, which were calculated compared to the as-prepared NiP coating as the control sample, as illustrated in the Equation below (Eq. (6)).

$$I.E. = \left[\frac{i_{corr(NiP)} - i_{corr(HNT)}}{i_{corr(NiP)}} \right] \times 100 \% \qquad (6)$$

where $i_{corr(NiP)}$ and $i_{corr(HNT)}$ linked to the corrosion current densities for the NiP coating and different HNTs nanocomposite coatings, respectively.

As elucidated from Tafel data (Fig. 15a and Table 5), E_{corr} of the NiP coating is −654 mV, while E_{corr} for the NiP/HNT coating is noticeably moved to the noble direction reaching - 467 mV. In addition, the NiP/HNT coating decreases the i_{corr} value about 2.6 times compared to that of the HNT-free coating,
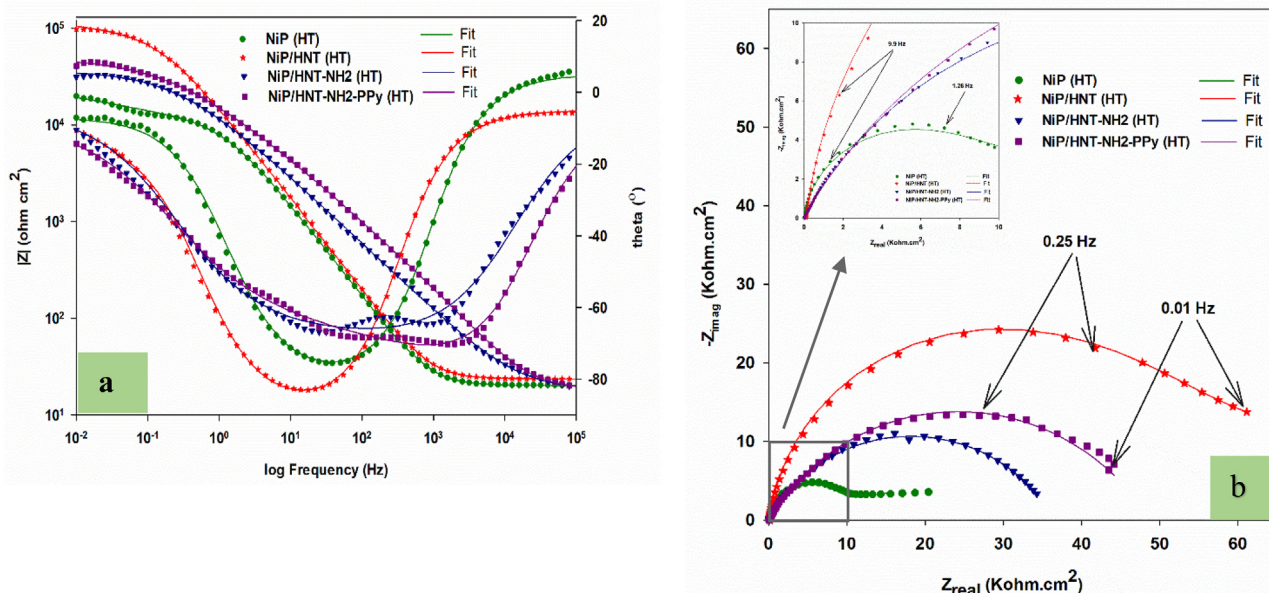
Fig. 14 – (a) Bode/phase angle and **(b)** Nyquist plots of the different heat-treated NiP nanocomposite coatings immersed in 3.5 wt % NaCl solution at room temperature.

indicating good protection ability due to the presence of HNTs. Furthermore, the Tafel curve of the modified NiP/HNT nanocomposite coating with NH$_2$ (NiP/HNT-NH$_2$) compared to the HNT−free coating' curve displays a successful increase in its E_{corr} associated with a decrease in its i_{corr}, suggesting an improvement in the corrosion resistance of the NiP coating in the presence of HNT-NH$_2$. Further modification of HNT-NH$_2$ with PPy leads to further minimizing the i_{corr} of the nanocomposite coating about 1.6 times in comparison to the modified one with NH$_2$ only, as shown in Fig. 15a and Table 5. Hence, the NiP/HNT−NH$_2$−PPy nanocomposite coatings have the highest corrosion protection efficiency, getting 85.9%, compared to the as-prepared NiP, as shown in Table 5. As previously mentioned, this is attributed to the presence of the conducting polymer (PPy) and the Ag atom, which have an acceptable protection behavior for the steel.

Unexpectedly, the heat-treated NiP, NiP/HNT, and its modifications nanocomposite coatings showed increasing and decreasing trends in their i_{corr} values compared to those of their corresponding as-prepared ones. Nonetheless, their E_{corr} is further moved to the positive direction, and their i_{corr} were smaller, as shown in Table 5. This illustrates that the different coatings' corrosion resistance has significantly enhanced after heat treatment. As clarified in Fig. 15b and

Table 5, the i_{corr} of the heat-treated NiP is almost 74.8% lower than the corresponding as-prepared one. Markedly, the NiP/HNT nanocomposite coating has the smallest i_{corr} (0.28 μAcm^{-2}), displaying superior protection efficiency of about 95%. This is due to the extra compactness of the heat-treated NiP/HNT nanocomposite coating, as clarified in SEM results concerning the modified HNT ones. Contrary to the as-prepared one, the heat-treated NiP/HNT-NH$_2$ and NiP/HNT−NH$_2$−PPy nanocomposite coatings displayed high i_{corr} values compared to the non-modified one (NiP/HNT), referring to a reduction in their protection efficiencies about 11.7% and 5.3%, respectively. This may be due to the degradation of the organic part of these composites after heat treatment at a high temperature, 400 °C, for a long time, 1 h. However, they still have about 8.7% and 15% higher protection efficiencies than the heat-treated HNT-free coating. It is valuable to mention that the results acquired from the electrochemical Tafel analysis agree with the outcomes of EIS technique.

3.2.6. Electroless co-deposition of the pristine and modified HNTs mechanism

Generally, many researchers have extensively researched and discovered the mechanism of the electroless deposition of NiP coating reaction, making it significantly develop in various

Table 4 – EIS fitting results of the different heat-treated NiP nanocomposite coatings immersed in 3.5 wt % NaCl solution at room temperature.

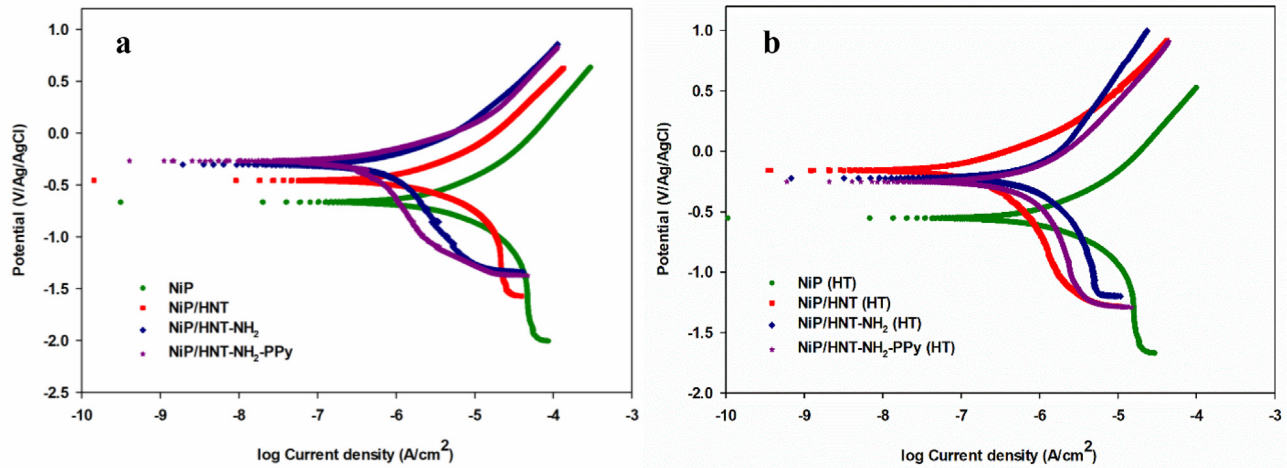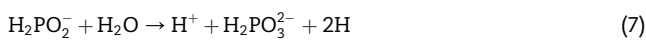| Coatings (heat-treated)	Rs ($\Omega \cdot$cm^2)	R_{po} ($\Omega \cdot$cm^2)	CPE$_{coat}$ (μF cm^{-2} S^{-n})	W (S.s$^{1/2}$)	R_p ($\Omega \cdot$cm^2)	CPE$_{dl}$ (μF$\cdot$cm^{-2} S^{-n})	n	I.E. (%)
NiP	16.0	3186	158	7.30	30,100	141	0.84	71.4
NiP/HNT	16.0	6570	7.50	–	82,170	2.16	0.96	89.5
NiP/HNT-NH$_2$	18.5	4087	19.5	–	45,280	15.4	0.96	81.0
NiP/HNT−NH$_2$−PPy	18.0	5260	18.6	–	58,020	15.6	0.96	85.2

Fig. 15 – Tafel plots of the different a) as-prepared and b) heat-treated nanocomposite coatings.

industrial applications [80–82]. The primary basis of the kinetics of the electroless NiP coatings is the metal surface production and adsorption of atomic hydrogen capacities. After that, the reduction of Ni^{2+} and hypophosphite ions and the co-deposition of nickel and phosphorus onto a metal surface. For NiP nanocomposite coatings, the second phase's physical adsorption occurred during the co-depositing of the Ni and P, as illustrated in the schematic diagram in Fig. 16.

Eqs. (7)–(9) describe the complete chemical reactions that occur during the electroless NiP deposition. Eq. (7) describes the reaction of the hypophosphite ions with the water molecules, which produces atomic hydrogen that is adsorbed onto the metal surface, creating an active site for the co-depositing of the Ni–P. Meanwhile, the reduction of the hypophosphite and nickel ions in the bath is done by the atomic hydrogen, as described by Eqs. (8) and (9), which produces co-depositing nickel-phosphorus (NiP) that is adsorbed on the substrate replacing the present atomic hydrogen. After that, the new atomic hydrogen is adsorbed into the NiP deposit, followed by the new co-deposition of Ni and P. Lastly, consumption of the produced H_{ads} occurs, and the Ni and P are successfully co-deposited, forming a thickness of NiP coating.

$$H_2PO_2^- + H_2O \rightarrow H^+ + H_2PO_3^{2-} + 2H \tag{7}$$

$$Ni^{2+} + 2H \rightarrow Ni + 2H^+ \tag{8}$$

$$H_2PO_2^- + H \rightarrow H_2O + OH^- + P \tag{9}$$

Throughout the mechanism of the electroless deposition of the NiP coatings, the physical deposition of the pristine or modified HNTs (HNT-NH$_2$ and HNT–NH$_2$–PPy) occurs. A two-step adsorption mechanism occurs for the co-deposition of the added materials. The transportation of the dispersed particles (HNTs or HNT-NH$_2$ or HNT–NH$_2$–PPy) in the bath to the electrode surface through mechanical action, followed by their physical adsorption due to the fluidal attack, is the first step. For the second step, the dehydration of the physically adsorbed occurs due to the irreversible chemical adsorption on the substrate and the strong electric field of the Helmholtz layer of the electrode, followed by the embedding of the adsorbed materials by reduced alloys or metals [83]. In order to improve the quality of the electroless NiP nanocomposite coatings and prevent the agglomeration of the HNTs and their modified particles in the suspension, ultra-agitation should be followed. Thus, their surfaces should be upward oriented to ease their occlusion in the deposit [84].

The outline of the electrochemical mechanism for the NiP plating is shown below [Eqs. (10)–(12)], under the assumption that catalytic oxidation occurs to the hypophosphite ions, while reduction occurs to the nickel and hydrogen ions along the catalytic surface.

Anodic reaction:

Table 5 – Tafel fitting results of the different a) as-prepared and b) heat-treated nanocomposite coatings.

Coating	$-E_{corr}$ (mV)	i_{corr} (μAcm^{-2})	b_a (V/decade)	b_c (V/decade)	I.E. (%)
NiP	654	5.74	0.54	0.18	—
NiP/HNT	467	2.19	0.32	0.27	61.8
NiP/HNT-NH$_2$	313	1.30	0.34	0.18	77.3
NiP/HNT–NH$_2$–PPy	247	0.81	0.15	0.14	85.9
NiP (HT)	518	1.45	0.21	0.16	74.7
NiP/HNT (HT)	156	0.28	0.16	0.13	95.1
NiP/HNT-NH$_2$ (HT)	232	0.95	0.13	0.18	83.4
NiP/HNT–NH$_2$–PPy (HT)	251	0.58	0.16	0.13	89.8
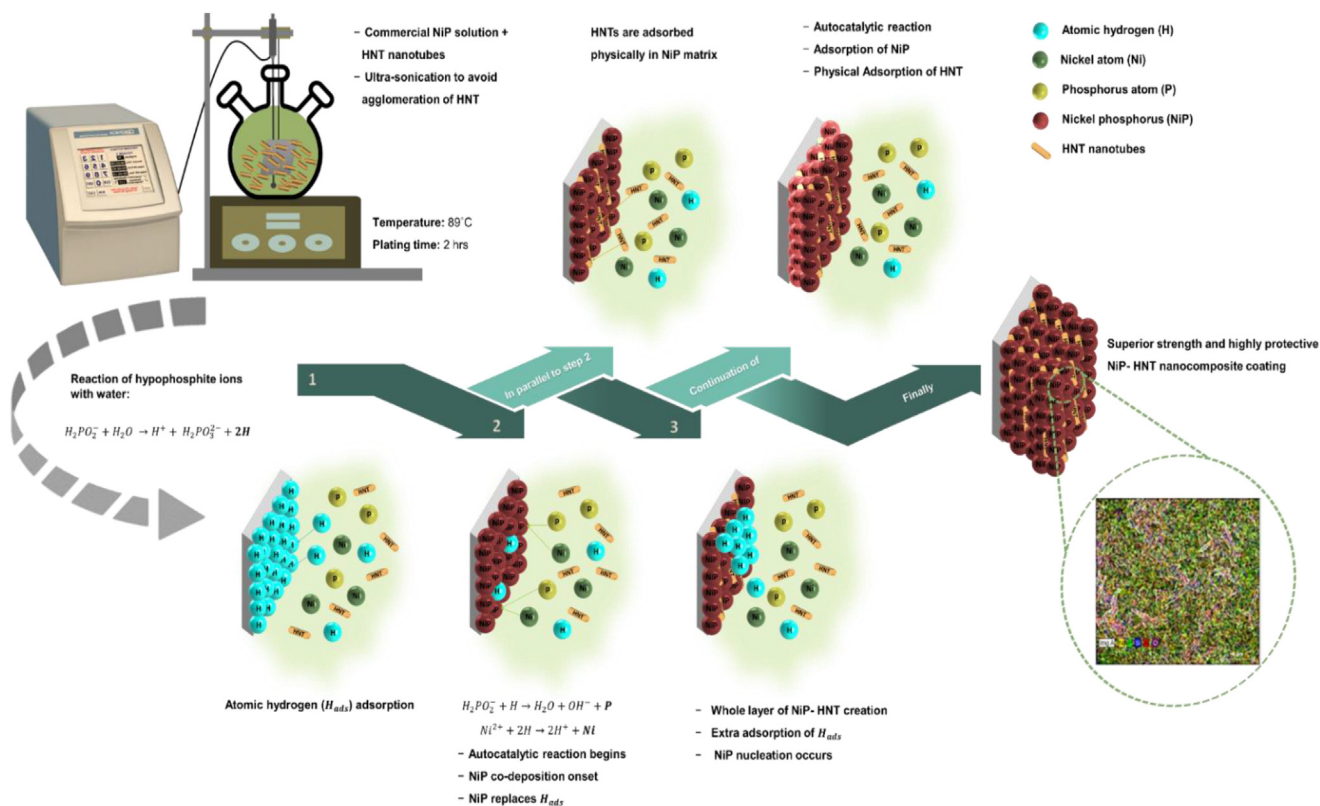
Fig. 16 – Schematic diagram for the electroless deposition of NiP/HNT nanocomposite coatings.

$$H_2PO_2^- + H_2O \rightarrow 2H^+ + H_2PO_3^- + 2e^- \tag{10}$$
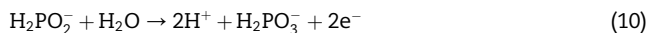
Cathodic reaction:

$$Ni^{2+} + 2e^- \rightarrow Ni \tag{11}$$

$$2H^+ + 2e^- \rightarrow H_2 \tag{12}$$

4. Conclusion

The pristine (HNTs) and modified HNTs (HNT-NH$_2$ and HNT−NH$_2$−PPy) were successfully introduced in the NiP matrix electroless-deposited with good adherence on the steel. Microscopic mapping images distinctly identified the uniform distribution of the HNTs. SEM and XRD measurements demonstrated the compact, fine-grained, crystalline structure of HNT nanocomposite coatings, especially after heat treatment. The hardness and electrochemical measurements revealed that adding HNTs in the NiP coating causes remarkable mechanical and corrosion resistance enhancement. The hardness and corrosion protection of the NiP coating were greatly enriched through the insertion of the modified HNT with either NH$_2$ or NH$_2$-PPy particles. Noteworthily, the heat treatment of different HNT nanocomposite coatings (NiP/HNT, NiP/HNT-NH$_2$, NiP/HNT−NH$_2$−PPy) led to further significant improvements in their hardness and corrosion protection efficiency. Subsequently, it is highly recommended to use NiP/HNT nanocomposite and their modified coatings as highly protective coating in chloride solution with better mechanical properties.

Declaration of competing interest

The authors declare that they have no known competing financial interests or personal relationships that could have appeared to influence the work reported in this paper.

Appendix A. Supplementary data

Supplementary data to this article can be found online at https://doi.org/10.1016/j.jmrt.2023.04.227.

REFERENCES

[1] Wang C, Farhat Z, Jarjoura G, Farhat MK, Abdullah AM, Fayyad EM. Investigating fracture behavior of annealed electroless Ni-P coating on pipeline steel using acoustic emission methodology. Surf Coat Technol 2017;326:336—42. https://doi.org/10.1016/j.surfcoat.2017.07.067.

[2] Fayyad EM, Abdullah AM, Hassan MK, Mohamed AM, Jarjoura G, Farhat Z. Recent advances in electroless plated Ni-P and its composites for erosion and corrosion applications: a review. Emergent Mater 2018;1(1):3—24. https://doi.org/10.1007/s42247-018-0010-4.

[3] Ashassi-Sorkhabi H, Es0 haghi M. Corrosion resistance enhancement of electroless Ni—P coating by incorporation of ultrasonically dispersed diamond nanoparticles. Corrosion Sci 2013;77:185—93. https://doi.org/10.1016/j.corsci.2013.07.046.

[4] Lelevic, A. Ni-P coatings electroplating-A review, Part I: pure Ni-P alloy. arXiv 2018, arXiv:1807.04693.

[5] Sudagar J, Lian J, Sha W. Electroless nickel, alloy, composite and nano coatings - a critical review. J Alloys Compd 2013;571:183—204. https://doi.org/10.1016/j.jallcom.2013.03.107.

[6] Balaraju JN, Raman N, Manikandanath NT. Nanocrystalline electroless nickel poly-alloy deposition: incorporation of W and Mo. Trans. IMF. 2014;92:169—76. https://doi.org/10.1179/0020296713Z.000000000123.

[7] Sadeghzadeh-Attar A, AyubiKia G, Ehteshamzadeh M. Improvement in tribological behavior of novel sol-enhanced electroless Ni-P-SiO2 nanocomposite coatings. Surf Coating Technol 2016;307:837—48. https://doi.org/10.1016/j.surfcoat.2016.10.026.

[8] Karthiekeyan S, Ramamoorthy B. Effect of reducing agent and nano Al2O3 particles on the properties of electroless Ni-P coating. Appl Surf Sci 2014;15:654—60.

[9] de Oliveira MCL, Correa OV, Ett B, Sayeg IJ, de Lima NB, Antunes RA. Influence of the tungsten content on surface properties of electroless Ni-W-P coatings. Mater Res 2017;21:1—13. https://doi.org/10.1590/1980-5373-MR-2017.

[10] Fayyad Eman M, Abdullah Aboubakr M, Hassan Mohammad K, Mohamed Adel M, Wang Chuhong. George jarjoura, zoheir farhat, synthesis, characterization, and application of novel Ni-P-carbon nitride nanocomposites. Coatings 2018;8:37.

[11] Fayyad EM, Abdullah AM, Mohamed AMA, Jarjoura G, Farhat Z, Hassan MK. Effect of electroless bath composition on the mechanical, chemical, and electrochemical properties of new NiP—C3N4 nanocomposite coatings. Surf Coat Technol 2019;362:239—51.

[12] Chen YI, Duh JG. TiN coatings on mild steel substrates with electroless nickel as an interlayer. Surf Coat Technol 1991;48:163—8.

[13] Chen W, Gao W, He Y. A novel electroless plating of Ni-P-TiO2 nanocomposite coatings. Surf Coat Technol 2010;204:2493—8.

[14] Allahkaram SR, Zarebidaki A, Rabizadeh T. Evaluation of electroless Ni-P and Ni-P nanocomposite coatings' properties. Int. J. Mod. Phys. Conf. Ser. 2012;5:817—24.

[15] Ranganatha S, Venkatesha TV. Fabrication and anticorrosion performance of Ni—P—B.N. nanocomposite coatings on mild steel. Surf Eng Appl Electrochem 2017;53:449—55.

[16] Fayyad Eman M, Abdul Rasheed P, Al-Qahtani Noora, Abdullah Aboubakr M, Hamdy Fatma, Sharaf Mohammed A, Hassan Mohammad K, Mahmoud Khaled A, Mohamed Adel M. George jarjoura, zoheir farhat, microbiologically-influenced corrosion of the electroless deposited NiP-TiNi — coating. Arab J Chem 2021;14:103445.

[17] Ahmadkhaniha D, Eriksson F, Leisner P, Zanella C. Effect of SiC particle size and heat-treatment on microhardness and corrosion resistance of NiP electrodeposited coatings. J Alloys Compd 2018;769:1080—7. https://doi.org/10.1016/j.jallcom.2018.08.013.

[18] Apachitei I, Tichelaar FD, Duszczyk J, Katgerman L. Solid-state reactions in low-phosphorus autocatalytic NiP— SiC coatings. Surf Coat Technol 2001;148:284—95.

[19] Ma C, Wu F, Ning Y, Xia F, Liu Y. Effect of heat treatment on structures and corrosion characteristics of electroless Ni—P—SiC nanocomposite coatings. Ceram Int 2014;40:9279—84.

[20] Erming M, Shoufu L, Pengxing L. A transmission electron microscopy study on the crystallization of amorphous Ni—P electroless deposited coatings. Thin Solid Films 1988;166:273—80.

[21] Chang CS, Hou KH, Der GM, Chung CK, Lin JF. Effects of annealing temperature on microstructure, surface roughness, mechanical and tribological properties of Ni—and Ni—P/SiC films. Surf Coat Technol 2016;288:135—43.

[22] Alirezaei S, Monirvaghefi SM, Salehi M, Saatchi A. Wear behavior of Ni—P and Ni—P—Al2O3 electroless coatings. Wear 2007;262:978—85.

[23] Liu M, Guo B, Du M, Cai X, Jia D. Properties of halloysite nanotube—epoxy resin hybrids and the interfacial reactions in the systems. Nanotechnology 2007;18:455703.

[24] Jana A, Bathula C, Park Y, Kadam A, Sree VG, Ansar S, Kim HS, Im H. Facile synthesis and optical study of organic-inorganic lead bromide perovskite-clay (kaolinite, montmorillonite, and Halloysite) composites. Surface Interfac 2022;1(29):101785.

[25] Li X, Jiang Y, Zhou R, Hou Z. Acetalization of glycerol with acetone over appropriately-hydrophobic zirconium organophosphonates. Appl Clay Sci 2020 May 1;189:105555.

[26] Setter OP, Segal E. Halloysite nanotubes—the nano-bio interface. Nanoscale 2020;12(46):23444—60.

[27] Wu H, Xu S, Lin K, Xu J, Fu D. Acidity-activatable dynamic halloysite nanotubes as a drug delivery system for efficient antitumor therapy. J Drug Deliv Sci Technol 2023;30:104208.

[28] Prabhu R, Shetty K, Jeevananda T, Murthy HA, Sillanpaa M, Nhat T. Novel polyaniline—halloysite nanoclay hybrid composites: synthesis, physico-chemical, thermal and electrical properties. 1 Inorg Chem Commun 2023;148:110328.

[29] Peng L, Xu Z, Chao L, Zheng D, Yang H, Sun C, Cui H. New energy-saving building developed by using polyethylene glycol/halloysite nanotube energy-storage blanket and heat-insulating glass with NaxWO3@ SiO2 nano-coating. Sol Energy Mater Sol Cell 2023;15:112074. 250.

[30] alvino MM, Lisuzzo L, Cavallaro G, Lazzara G, Pipitone C, Giannici F. Beeswax/halloysite microparticles embedded within a geopolymeric layer for the protective coating of steel. Mater Lett 2023;330:133257.

[31] Jouyandeh M, Karami Z, Jazani OM, Formela K, Paran SMR, Jannesari A. Curing epoxy resin with anhydride in the presence of halloysite nanotubes: the contradictory effects of filler concentration. Prog Org Coating 2019;126:129—35.

[32] Jouyandeh M, Tikhani F, Hampp N, Yazdi DA, Zarrintaj P, Ganjali MR, Saeb MR. Highly curable self-healing vitrimer-like cellulose-modified halloysite nanotube/epoxy nanocomposite coatings. Chem Eng J 2020;396:125196.

[33] Abdullayev E, Price R, Shchukin D, Lvov Y. Halloysite tubes as nanocontainers for anticorrosion coating with benzotriazole. Applied Materials and Interfaces 2009;7:1437—43.

[34] Shchukin DG, Lamaka SV, Yasakau KA, Zheludkevich ML, Ferreira MGS, Mohwald H. Active anticorrosion coatings with halloysite nanocontainers. J Phys Chem C 2008;112:958—64.

[35] Ranganatha S, Venkatesha TV, Vathsala K. Development of high performance electroless Ni—P—HNT composite coatings. Appl Surf Sci 2012;263:149—56.

[36] Jlassi K, Mallick S, Mutahir H, Ahmad Z, Touati F. Synthesis of in situ photoinduced halloysite-Polypyrrole@Silver nanocomposite for the potential application in humidity sensors. Nanomaterials 2020;10(7):1426.

[37] Saad A, Bakas I, Piquemal J-Y, Nowak S, Abderrabba M, Chehimi MM. Mesoporous silica/polyacrylamide composite: preparation by UV-graft photopolymerization, characterization and use as Hg (II) adsorbent. Appl Surf Sci 2016;367:181—9.

[38] Jlassi K, Singh A, Aswal DK, Losno R, Benna-Zayani M, Chehimi MM. Novel, ternary clay/polypyrrole/silver hybrid materials through in situ photopolymerization. Colloids Surf A Physicochem Eng Asp 2013;439:193—9.

[39] Saugo M, Flamini DO, Brugnoni LI, Saidman SB. Silver deposition on polypyrrole films electrosynthesised onto Nitinol alloy. Corrosion protection and antibacterial activity. Mater Sci Eng C 2015 Nov 1;56:95—103.

[40] Jouyandeh M, Jazani OM, Navarchian AH, Shabanian M, Vahabi H, Saeb MR. Bushy-surface hybrid nanoparticles for developing epoxy super adhesives. Appl Surf Sci 2019;479:1148—60.

[41] Jlassi K, Benna-Zayani M, Chehimi M, Yagci Y. Efficient photoinduced in situ preparation of clay/poly(glycidyl methacrylate) nanocomposites using hydrogen-donor silane. Plym Chem 2015;53(6):800—8.

[42] Jlassi K, Chandran S, Poothanari MA, Benna-Zayani M, Thomas S, Chehimi MM. Clay/polyaniline hybrid through diazonium chemistry: conductive nanofiller with unusual effects on interfacial properties of epoxy nanocomposites. Langmuir 2016 Apr 12;32(14):3514—24.

[43] Raos B, Doyle C, Simpson M, Graham E, Unsworth C. Selective PEGylation of parylene-C/SiO$_2$ substrates for improved astrocyte cell patterning. Sci Rep 2018;8(1):1—11.

[44] Jlassi K, et al. Anti-corrosive and oil sensitive coatings based on epoxy/polyaniline/magnetite-clay composites through diazonium interfacial chemistry. Sci Rep 2018;8(1):1—13.

[45] Jlassi K, Chehimi MM, Thomas S. Clay-polymer nanocomposites. Elsevier; 2017.

[46] W. Sade, R. TrindadeProenc, T.D.O. Moura, J.R.T. Branco, Electroless Ni-P coatings: preparation and evaluation of fracture toughness and scratch hardness, ISRN Materials Science Volume 2011, Article ID 693046, 6 pages, doi:10.5402/2011/693046.

[47] Buchtík M, Kosár P, Wasserbauer J, Tkacz J, Doležal P. Characterization of electroless Ni—P coating prepared on a wrought ZE10 magnesium alloy. Coatings 2018;8:96. https://doi.org/10.3390/coatings8030096.

[48] Novakovic J, Vassiliou P. Vacuum thermal treated electroless NiP—TiO2 composite coatings. Electrochim Acta 2009;54:2499—503.

[49] Radhi NS, Marza M, Al-Khafaji ZS. Modification of nickel-phosphor electroless coatings by adding particles of zirconia. Solid State Technol 2020;63(2):1178—86.

[50] Sharma S, Sharma S, Agarwala P, Garg R, Gopinath P. A study on Ni-P and Ni—P—ZnO composite coatings developed by electroless technique. Adv Mater Res 2012;585:512—6.

[51] Farhan M, Fayyaz O, Nawaz M, Radwan AB, Shakoor RA. Synthesis and properties of electroless Ni—P—HfC nanocomposite coatings. Mater Chem Phys 2011;291:126696—709.

[52] Khaira A, Shown I, Samireddi S, Mukhopadhyay S, Chatterjee S. Mechanical and tribological characterization of deep eutectic solvent assisted electroless Ni—P-hBN coating. Ceram Int 2023;49:461—73.

[53] Li Z, Farhat Z, Jarjoura G, Fayyad E, Abdullah A, Hassan M. Synthesis and characterization of scratch-resistant Ni-P-Ti-based composite coating. Tribol Trans 2019;62(5):880—96.

[54] MacLeana M, Farhat Z, Jarjoura G, Fayyad E, Abdullah A, Hassan M. Fabrication and investigation of the scratch and indentation behavior of new generation Ni-P-nano-NiTi composite coating for oil and gas pipelines. Wear 2019;426—427:265—76.

[55] Novakovic J, Vassiliou P, Samara Kl, Argyropoulos Th. Electroless NiP—TiO$_2$ composite coatings: their production and properties. Surf Coat Technol 2006;201:895—901.

[56] Wu YC, Li GH, Zhang L. Wear resistance of electroless deposited Ni—P and Ni—P/SiC composite coatings on low alloy cast iron. Surf Eng 2000;16(6):506—10.

[57] Balarajui JN, Sankara Narayanan TSN, Seshadri SK. Electroless Ni—P composite coatings. J Appl Electrochem 2003;33:807—16.

[58] Xiang Y, Zhang J, Jin C. Study of electroless Ni-P-nanometer diamond composite coatings. Plat Surf Finish 2001;88(2):64—7.

[59] Qipeng LV, Huang Mingliang, Zhang Shaoqian, Deng Songwen, Gong Faquan, Wang Feng, Pan Yanwei, Li Gang, Jin Yuqi. Effects of annealing on residual stress in Ta$_2$O$_5$ films deposited by dual ion beam sputtering. Coatings 2018;8:150. https://doi.org/10.3390/coatings8040150.

[60] Fayyad Eman M, Abdullah Aboubakr M, Hassan Mohammad K. Kashif rasool, khaled A mahmoud, adel mohamed, george jarjoura, zoheir farhat, novel electroless—deposited NiP—TiNi nanocomposite coatings for anti-corrosion and anti—bacterial applications. Surf Coating Technol 2019;369:323—33.

[61] Karthikeyan S, Vijayaraghavan L. Investigation of the surface properties of heat—treated electroless Ni—P coating. Trans. IMF 2016;94:265—73.

[62] Jiang B, Jiang SL, Ma AL, Zheng YG. Effect of heat treatment on erosion—corrosion behavior of electroless Ni—P coatings in saline water. Mater Manuf Process 2014;29:74—82.

[63] Abdel Aal A. Hard and corrosion resistant nanocomposite coating for Al alloy. Mater Sci Eng 2008;474:181—7.

[64] Li W, Mao J, Feng J. Aluminum gain refinement by Ti(C,N) nanoparticles additions: principles, advantages, and drawbacks. Metall Res Technol. 2019;116.

[65] Song Y, Yeon J, Na B. Numerical simulation of the Hall-Petch relationship in aluminium using gradient-enhanced plasticity model. Adv Civ Eng 2019;2019.

[66] Sadreddini S, Afshar A. The effect of heat treatment on properties of Ni—SiO2 nano composite coating. Protect Met Phys Chem Surface 2016;52(3):492—9.

[67] Rabizadeh T, Allahkaram SR, Zarebidaki A. An investigation on effects of heat treatment on corrosion properties of Ni—P electroless nano—coatings. Mater Des 2010;31:3174—9.

[68] Singh DRP, Chawla N, Tang G, Shen Y—L. Anomalous viscoplasticity during nanoindentation of Al/SiC nanolaminated composites. Mater Sci Eng, A 2011;528:4608—14.

[69] Mehdi R, Naser E, Nader P, Baharvandi HR. The effect of sintering temperature and the amount of reinforcement on the properties of Al—Al2O3 composite. Mater Des 2008;30:3333—7.

[70] Kim HS, Hong SI, Kim SJ. On the rule of mixtures for predicting the mechanical properties of composites with homogeneously distributed soft and hard particles. J Mater Process Technol 2001;112:109—13.

[71] Kim HS. On the rule of mixtures for the hardness of particles reinforced composites. Mater Sci Eng 2000;A289:30—3.

[72] Su C, Wu W, Li Z, Guo Y. Prediction of film performance by electrochemical impedance spectroscopy. Corrosion Sci 2015;99:42—52. https://doi.org/10.1016/j.corsci.2015.05.029.

[73] Fayyad EM, Almaadeed MA, Jones A, Abdullah AM. Evaluation techniques for the corrosion resistance of self-healing coatings. Int J Electrochem Sci 2014;9(9):4989—5011.

[74] Shahzad K, et al. Corrosion and heat treatment study of electroless nip-ti nanocomposite coatings deposited on HSLA steel. Nanomaterials 2020;10(10):1—19. https://doi.org/10.3390/nano10101932.

[75] Nguyen AS, Musiani M, Orazem ME, Pébère N, Tribollet B, Vivier V. Impedance study of the influence of chromates on the properties of waterborne coatings deposited on 2024 aluminium alloy. Corrosion Sci 2016;109:174—81. https://doi.org/10.1016/j.corsci.2016.03.030.

[76] Xu J, Zhang L, Shi R, Zhu Y. Chemical exfoliation of graphitic carbon nitride for efficient heterogeneous photocatalysis. J Mater Chem 2013;1(46):14766—72. https://doi.org/10.1039/c3ta13188b.

[77] Gad El-Rab SMF, Fadl-allah SA, Montser AA. Improvement in antibacterial properties of Ti by electrodeposition of biomimetic Ca—P apatite coat on anodized titania. Appl Surf Sci 2012;261:1—7. https://doi.org/10.1016/j.apsusc.2012.05.139.

[78] Benoit M, et al. Comparison of different methods for measuring the passive film thickness on metals. Electrochim Acta 2016;201:340—7. https://doi.org/10.1016/j.electacta.2015.12.173.

[79] Rabizadeh T, Allahkaram SR, Zarebidaki A. An investigation on effects of heat treatment on corrosion properties of Ni-P electroless nano-coatings. Mater Des 2010;31(7):3174—9. https://doi.org/10.1016/j.matdes.2010.02.027.

[80] Gould A, Boden PJ, Harris SJ. Phosphorus distribution in electroless nickel deposits. Surf Technol 1981;12:93—102.

[81] Bielinski J. Oberflache Surface 1984;5:423.

[82] Riedel W. Electroless nickel plating. Liverpool: Redwood Press Limited; 1991.

[83] Balaraju JN, Rajam KS. Electroless deposition and characterization of high phosphorus Ni—P—Si$_3$N$_4$ composite coatings. Int J Electrochem Sci 2007;2:747—61.

[84] Xiang YW, Zhang JY, Jin CH. Plat Surf Finish 2001;88(2):64.